Case Studies in Thermal Engineering 87 (2026) 108634

Contents lists available at ScienceDirect

Case Studies in Thermal Engineering

journal homepage: www.elsevier.com/locate/csite

Experimental and theoretical performance analysis of building-integrated photovoltaic and thermal system

Heon-Min Lee [a,b], Youngsub An [a], Ye-Bin Shin [a,b], Wong-Jong Choi [a,b], ByungKi Jeon [a], Jongkyu Kim [a], Jae-Weon Jeong [b], Min-Hwi Kim [a,*]

[a] Renewable Energy System Laboratory, Korea Institute of Energy Research, 152 Gajeong-ro, Yuseong-gu, Daejeon, 34129, Republic of Korea
[b] Department of Architectural Engineering, College of Engineering, Hanyang University, 222, Wangsimni-Ro, Seongdong-Gu, Seoul, 04763, Republic of Korea

GRAPHICAL ABSTRACT

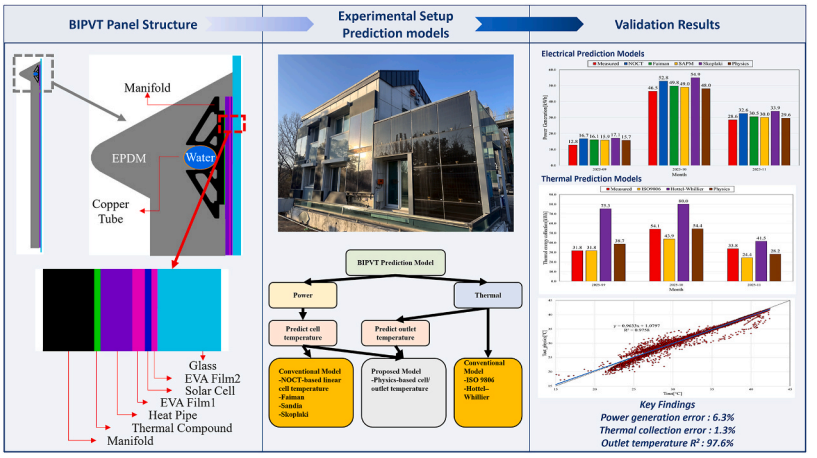

ARTICLE INFO

Keywords:
BIPVT
Energy self-sufficiency
Power generation
Thermal energy collection

ABSTRACT

This study presents an experimental and modeling-based performance assessment of a frameless, curtain-wall-type building-integrated photovoltaic and thermal system under real operating conditions. Specifically, eight modules (each 1 m^2 in area and constituting 8 m^2 in total area) were installed on the south-facing façade of the zero-energy performance test house and operated

* Corresponding author.
E-mail address: mhkim001@kier.re.kr (M.-H. Kim).

https://doi.org/10.1016/j.csite.2026.108634
Received 9 February 2026; Received in revised form 28 September 2026; Accepted 14 October 2026
Available online 19 October 2026
2214-157X/© 2026 The Authors. Published by Elsevier Ltd. This is an open access article under the CC BY-NC license (http://creativecommons.org/licenses/by-nc/4.0/).

Heat-transfer mechanism
Prediction model
Zero-energy building

from 1 September to 8 November 2025 to replicate winter operations. Field measurements were recorded of vertical-plane irradiance, ambient temperature, inlet/outlet fluid temperatures, flow rate, and inverter-based power generation at 1-min intervals. Under clear-sky conditions, the system achieved peak power and thermal energy collection values of 1100 and 9049.8 W, respectively. Moreover, the highest cumulative power generation and thermal energy collection over the entire monitoring period were 87.9 and 119.6 kWh, respectively. For evaluations of the prediction accuracy, four electrical models (namely, nominal operating cell temperature-based, Faiman, Sandia array performance, and Skoplaki) and two thermal models (ISO 9806 and Hottel–Whillier) were implemented and compared under identical boundary conditions. Additionally, a novel physics-based coupled model for cell and outlet fluid temperature was proposed and validated. This model, explicitly factoring multilayer conduction and cell–tube–fluid heat exchange, achieved the lowest cumulative errors of 6.3% and 1.3% for electricity and heat, respectively, with a coefficient of determination (R^2) of 0.975. Notably, although the experimental period is limited to the winter season, the results demonstrate that resolving internal heat-transfer mechanisms improves the predictive accuracy of building-integrated photovoltaic and thermal systems significantly.

Nomenclature

Symbols	
A	Module area, m^2
A_{pipe}	Effective heat transfer area for tube-fluid heat exchange, m^2
$A_{pipe,con}$	Tube area contributing to heat exchange in the connection section, m^2
$A_{pipe,hex}$	Tube area contributing to heat exchange in the module-pass section, m^2
a	Sandia module temperature model coefficient
a_1	Linear heat loss coefficient, W/(m^2•K)
b	Wind speed coefficient, $(m/s)^{-1}$
C_p	Specific heat capacity of the heat-transfer fluid, J/(kg•K)
D	Tube inner diameter, m
E_0	Reference irradiance, W/m^2
F'	Collector efficiency factor
F_R	Heat removal factor
$h_{conv,ext}$	External convective heat transfer coefficient, W/(m^2•K)
$h_{conv,HW}$	Hottel–Whillier's internal convective heat transfer coefficient, W/(m^2•K)
$h_{conv,fluid}$	Internal convective heat transfer coefficient, W/(m^2•K)
I_v	Vertical-plane irradiance, W/m^2
k	Thermal conductivity of the fluid, W/(m•K)
k_i	Thermal conductivity of layer i, W/(m•K)
L_i	Thickness of layer i, m
$\dot{m}$	Mass flow rate, kg/s
N	Number of samples
n	Number of modules
Nu	Nusselt number
$P_{measured}$	Measured power generation, W
P_{model}	Power generation calculated using predicted model, W
Pr	Prandtl number
$Q_{Hottel-Whillier}$	Thermal energy collection rate predicted by Hottel–Whillier model, W
$Q_{ISO9806}$	Thermal energy collection rate predicted by ISO 9806 model, W
$Q_{measured}$	Measured thermal energy collection rate, W
$Q_{physics}$	Thermal energy collection rate predicted by physics-based model, W
$R_{back,total}$	Thermal resistance of the rear side total layer, m^2•K/W
$R_{b\rightarrow tube}$	Thermal resistance between the back plate and tube, m^2•K/W
Re	Reynolds number
$R_{f\rightarrow cell}$	Thermal resistance from the front surface to the PV cell, m^2•K/W
R_i	Areal thermal resistance of layer i, m^2•K/W
R_{total}	Total area thermal resistance across the multilayer stack, m^2•K/W
T_{amb}	Ambient air temperature, °C
T_b	Back surface temperature, °C
T_{cell}	Cell temperature, °C
$T_{cell,Faiman}$	Faiman model cell temperature, °C
$T_{cell,NOCT}$	Nominal operating cell temperature model-based cell temperature, °C
$T_{cell,physics}$	Physics-based predicted cell temperature, °C
$T_{cell,SAPM}$	Sandia cell temperature, °C
$T_{cell,Skoplaki}$	Skoplaki cell temperature, °C
T_f	Front surface temperature, °C
T_{in}	Inlet temperature, °C
T_{NOCT}	Nominal operating cell temperature, °C
T_{out}	Outlet temperature, °C

(*continued on next page*)

(*continued*)

Symbols	
$T_{out,physics}$	Physics-based predicted outlet temperature, °C
T_{ref}	Reference temperature, °C
T_{SAPM}	Sandia module back-surface temperature, °C
T_{sky}	Sky radiative temperature, °C
T_{tube}	Copper tube temperature, °C
U_0	Combined heat loss coefficient, W/(m^2•K)
U_1	Wind-dependent heat loss coefficient, W/(m^2•K•(m/s))
U_L	Overall collector heat loss coefficient (Hottel–Whillier model), W/(m^2•K)
V	Volumetric flow rate, L/min
x	Measured value of the variable
$\overline{x}$	Sample mean of x
ΔT_{SAPM}	Cell-to-module temperature difference parameter, °C
$\Delta T_{Skoplaki}$	Cell temperature rise above ambient air temperature, °C
Greek symbols	
α	Solar absorptance of the PV cell
β	Temperature reduction coefficient,/°C
$\delta_{v,x}$	Combined absolute uncertainty
$\delta_{vr,x}$	Type An uncertainty component
$\delta_{ve,x}$	Type B uncertainty component
ε	Hemispherical emissivity
η_0	Optical efficiency of the collector
η_{ref}	Reference power generation efficiency
μ	Dynamic viscosity, Pa•s
v_{wind}	Wind speed, m/s
π	pi
σ	Stefan–Boltzmann constant, W/(m^2•K^4)
σ_x	Sample standard deviation of x
τ	Solar transmittance
ϕ	Diameter, mm
Abbreviations	
BIPV	Building-integrated photovoltaic
BIPVT	Building integrated photovoltaic thermal
EPDM	Ethylene propylene diene monomer
EVA	Ethylene-vinyl acetate
KOLAS	Korea laboratory accreditation scheme
KePSH	Energy-plus solar house
MAE	Mean absolute error
MFHP	Microchannel flat-plate heat pipe
NOCT	Nominal operating cell temperature
PLC	Programmable logic controller
PVT	Photovoltaic thermal
RMSE	Root mean square error
RTD	Resistance temperature detector
SAPM	Sandia array performance model

1. Introduction

The building sector, accounting for approximately 33% of total primary energy consumption, exerts a critical, influence on the achievement of carbon neutrality at a global level, and the realization of zero-energy buildings is essential to this end [1]. In the Republic of Korea, the government has spearheaded the lead in establishment of a roadmap for achieving mandatory zero-energy buildings, targeting energy-consumption reductions in major end-use sectors of commercial real estate namely heating, domestic hot water, cooling, lighting, and ventilation and to improve energy self-sufficiency improvement via renewable energy sources [2]. By 2030, public buildings featuring a total floor area of or exceeding 500 m^2 are required to achieve Zero Energy Building Grade 3 status (corresponding to an energy self-sufficiency rate of 60%–80%), and private buildings featuring a total floor area of or exceeding 500 m^2 must achieve Grade 5 status (corresponding to an energy self-sufficiency rate of 20%–40%) [2,3].

In this context, photovoltaic and thermal (PVT) systems have attracted increasing attention as a promising zero-energy technology because they simultaneously generate electricity and useful heat from the same solar input [4,5]. Conventional PVT systems are commonly installed on roofs; however, their applicability in high-rise buildings is limited because the available roof area does not increase with building height [5]. For this reason, building-integrated PVT (BIPVT) systems, which are incorporated into the building envelope, have recently been explored as an effective alternative for improving urban energy self-sufficiency [5,6]. In particular, vertically installed façade-based BIPVT systems can mitigate summer overheating due to reduced high-angle solar exposure while improving winter energy capture by intercepting low-angle solar radiation [6].

Moreover, summer months involve low thermal demands and lead to stagnations in PVT heat collection performance, owing to collector overheating and storage-tank temperature increases. Conversely, in the winter months involving high thermal demands, reduced solar irradiance leads to decreased electrical generation and thermal collection performance. To address these limitations,

recent studies have actively targeted on the development of building-integrated PVT (BIPVT) systems, wherein PVT systems are integrated into the building envelope [7,8].

Such integrated BIPVT systems function as a single envelope component. When installed vertically, they can reduce the risk of overheating in summer by mitigating high-altitude solar irradiance and improving increasing thermal energy collection in winter by better capturing low-altitude solar irradiance [5]. Therefore, these systems have garnered attention as a key technology for achieving energy self-sufficiency in zero-energy buildings, as they overcome the installation constraints and performance limitations of conventional PVT systems while simultaneously enabling energy collection by means of exploiting the entire building envelope.

As described above, BIPVT technology enables simultaneous electricity and heat production by exploiting the building envelope, and is therefore emerging as a key alternative for achieving zero-energy buildings and improving energy self-sufficiency. However, for quantitative evaluations of the practical applicability and design feasibility of BIPVT technology, simple presentation of experimental results are inadequate; instead, simulation models that can predict performance in advance under various climate conditions, operating strategies, and system configurations should be developed. Particularly, unlike conventional roof-mounted PVT systems, BIPVT systems feature vertical installation and integration with the building envelope, which are complex aspects. Therefore, various PVT simulation models should be compared to identify those that can appropriately capture electricity and thermal energy collection when applied to buildings.

Notably, electrical and thermal performance in BIPVT systems are not independent; instead, cell temperature, collector temperature, and heat recovery conditions are strongly interrelated. Cell temperature is a key indicator determining electrical efficiency while simultaneously influencing thermal energy collection; concurrently, the inlet temperature and flow rate of the collector influence the cell temperature during thermal operation [6]. As these electrical and thermal interactions prove difficult to adequately represent under independent analyses of single-purpose PV or solar thermal models, an integrated simulation approach factoring the unique heat-transfer mechanisms and operating characteristics of BIPVT technology is required. Accordingly, physical prediction models are also necessary for BIPVT simulations at the design stage.

Previous studies have proposed various cell-temperature prediction models for estimating PV power generation and thermal-performance models for evaluating solar-thermal collection performance. Most of these models were originally developed as empirical or performance-coefficient-based approaches for conventional PV or single solar-thermal systems. For PV power prediction, the nominal operating cell temperature (NOCT)-based model estimates cell temperature from a linear relationship between solar irradiance and ambient temperature [9]. Trinuruk et al. [10] and Martín-Chivelet et al. [11] showed that the NOCT-based model, SAPM, and Faiman model can provide reasonable accuracy for BIPV applications; however, these approaches were not developed for liquid-cooled BIPVT systems in which the working fluid directly modifies cell temperature. More recently, wall-type and frameless BIPVT studies have further highlighted that the heat recovery configuration and internal thermal resistance strongly influence both electrical and thermal performance [7,12,13]. Similarly, the ISO 9806 and Hottel-Whillier thermal models were originally derived for tilted flat-plate collectors and do not fully capture the multilayer conductive resistance and direct cell-to-fluid heat exchange inherent to façade-integrated BIPVT modules [14,15]. Accordingly, studies that simultaneously compare electrical and thermal prediction models for vertically installed, frameless curtain wall-type liquid BIPVT systems under identical operating boundary conditions remain scarce in the literature.

Over the past three years, research on facade-mounted BIPV and BIPVT systems has expanded to include feasibility assessments, changes in power output under various shading conditions, internal panel temperature distribution, PCM-based thermal management, convertible curtain wall structures, and PV/T coupled modeling. For example, research on facade-based BIPVT-PCM systems demonstrated that a structure incorporating a 12-mm vacuum gap and a low-emissivity absorber could maintain a supply water temperature of 45 °C for 5 min, thereby demonstrating the practical feasibility of heat storage and heat supply in exterior wall-mounted BIPVT systems [16]. Furthermore, an analysis of a BIPV prototype installed on an east-facing ventilated façade revealed that while anthracite-colored modules had higher STC-rated efficiency, green modules demonstrated superior performance under actual operating conditions, confirming that shading, module placement, and rear ventilation are key performance determinants in exterior wall systems [17]. A study on the annual energy analysis of semi-transparent solar thermal facades showed that cooling through adjacent air circulation can contribute to reducing PV temperatures and improving electrical efficiency [18], while a study on convertible BIPVT curtain walls reported that total heat and electricity production could be improved by 2% to 25% compared to a fixed intake configuration, emphasizing the importance of flow path control [19]. Furthermore, a full-scale BIPV facade case study demonstrated an annual energy harvest potential of 26,436 kWh/a for a south-facing facade, 31,723 kWh/a for the entire facade, and 83.6 kWh/m^2a, illustrating the feasibility of real-world building applications [20]. Meanwhile, a recent study systematically reviewed facade solar solutions and proposed application strategies based on climate conditions and design methods [21]. However, despite these recent studies, research that simultaneously compares the electrical performance and heat collection performance of vertical frameless water-cooled curtain wall BIPV systems under identical boundary conditions and contrasts these results with physics-based models remains limited.

To address these gaps, this study proposes and validates a novel physics-based coupled model for a frameless curtain wall-type liquid BIPVT system installed on the south-facing facade of the energy-plus solar house (KePSH-2) at the Zero Energy Performance Test Building of the Korea Institute of Energy Research [12,13]. Using measured data obtained under real operating conditions, power generation and thermal energy collection were systematically evaluated with four electrical prediction models the NOCT-based linear cell temperature model [9], Faiman model [22], Sandia Array Performance Model (SAPM) [23], and Skoplaki model [24] and two thermal collection models ISO 9806 [14] and Hottel–Whillier model [15]. Subsequently, power generation and thermal energy collection were systematically evaluated based on the measured data via multiple predictive models: four power generation models the NOCT-based linear cell temperature model [9], Faiman model [22], Sandia Array Performance Model (SAPM) [23], and Skoplaki

model [24] and two thermal collection models ISO 9806 [14] and Hottel–Whillier model [15]. Additionally, a novel physics-based coupled model is proposed that explicitly resolves multilayer conduction across the module cross-section and the cell-to-tube-to-fluid heat exchange pathway, enabling simultaneous predictions of the cell and outlet fluid temperatures without the need for empirical fitting to system-specific coefficients. Unlike previous studies that have applied electrical or thermal models independently, or validated them against non-integrated PV or flat-plate collector systems, this study provides a systematic comparison of multiple predictive models for a vertically installed, building-envelope-integrated liquid PVT system, directly quantifying the prediction errors attributable to the neglect of internal heat transfer-mechanisms. The outcomes of this study are expected to provide evidence-based guidance for model selection in BIPVT simulation and design; and support the broader implementation of facade-integrated solar energy systems in zero-energy building practice.

2. Methodology

2.1. BIPVT system overview

Fig. 1 illustrates the BIPVT system developed in a previous study [13]. Notably, the BIPVT investigated herein was designed on the basis of a frameless curtain-wall-type BIPV structure with the objective of its integration into the building envelope, and it was also configured as an integrated BIPVT system via incorporation of a solar thermal collection function. The aim was for the system to function simultaneously as an exterior finishing material and as insulation for the building façade, while producing both electricity and heat.

Notably, a crystalline silicon–based PV module was applied in this system. Tempered glass was applied on the front side to protect the PV cells, and the rear side featured an unglazed structure without additional glass. This configuration was adopted to ensure structural simplicity when applied to a curtain wall envelope and simultaneously recover heat efficiently.

For improved constructability and connection efficiency between modules, a heat recovery piping structure was applied wherein multiple BIPVT modules shared a single main pipe. Through this approach, issues such as piping complexity, construction difficulty, and increased thermal losses which might arise when configuring independent piping for each module were minimized.

For ensuring balanced flow distribution across the eight parallel modules without using individual balancing valves, the supply-and-return manifold was sized such that the pressure drop across the manifold headers was negligible relative to the pressure drop within each module branch. As all eight modules were geometrically identical with the same hydraulic resistance, such a manifold design enabled naturally uniform flow distribution under all operating conditions. The temperature difference between the inlet and outlet headers was monitored over repeated operating cycles during system operation to assess the potential performance impact of utilizing only a single extraction point per module. The measured temperature differential remained stable across the experimental period, confirming that the manifold configuration produced adequately balanced thermal extraction from each module.

For heat recovery, a microchannel flat-plate heat pipe (MFHP) was attached to the rear side of the BIPV module to effectively collect the heat generated from the PV cells. The MFHP was configured to transfer the heat generated in each module to the main pipe through a manifold, thereby improving the uniformity of heat recovery among modules and enhancing the overall heat-transfer efficiency of the system. An ethylene-vinyl acetate (EVA) film was applied at the interface between the MFHP and the BIPV module, and a thermal compound was applied at the interface between the MFHP and the heat pipe to enhance thermal conductivity.

The MFHP was positioned at the top rear section of each module following three primary considerations. First, for a vertically mounted curtain wall module, the upper portion of the module surface exhibited higher temperatures under low-wind conditions, as the heated boundary-layer air rising along the exterior glass surface accumulated at the top of the module. Positioning the MFHP at the top rear therefore enables preferential heat extraction from the highest-temperature zone, ultimately maximizing the temperature differential available for heat transfer to the circulating fluid. Second, the hydraulic circuit was designed to feature an upflow configuration wherein cooler supply fluid entered from the bottom manifold, rose through the interior of the module, and exited at the top into the return manifold; such upward flow direction suppressed air-pocket formation and ensured continuous single-phase liquid contact with the heat-exchange surface. Notably, the working fluid in this system operated entirely in the single-phase liquid regime, i.e., no phase change occurred within the operating temperature range, gravity-assisted condensate return was not a relevant mechanism to consider, and the top placement was determined solely based on the thermal gradient and hydraulic considerations described above. Third, as the frameless curtain wall system featured concentrated structural attachment hardware along the top and bottom rails, routing the MFHP hydraulic connections through the top structural rail allowed for the piping to be concealed within the frame without penetration the glazed cell area, whereby the architectural continuity of the building façade could be preserved.

Through this configuration, the BIPVT system developed herein was designed to simultaneously perform the functions of a building envelope, power generation and thermal collection. A curtain wall-type BIPVT system was adopted to allow for multiple modules to operate collectively while minimizing the number of joints. As these structural and thermal characteristics prove difficult to represent adequately using conventional simple empirical models when predicting power generation and thermal collection, this study involved the development and validation of simulation models factored take these characteristics.

2.2. Simulation model

The models employed herein to predict the electrical-power generation and thermal energy collection performance of the BIPVT module are depicted in Fig. 2. In general, power generation prediction commonly involves the use of NOCT-based linear empirical cell temperature models; however, in PVT systems, these models cannot predict changes in cell temperature resulting from collector

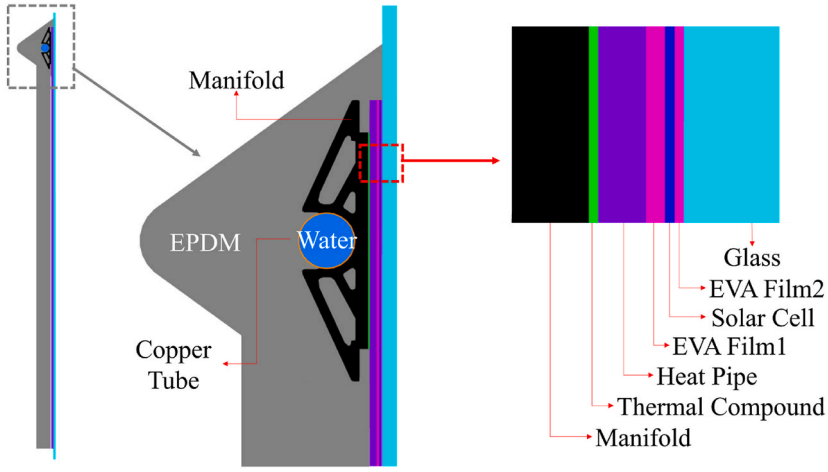

(a) Sectional view



(b) Prototype panel front view

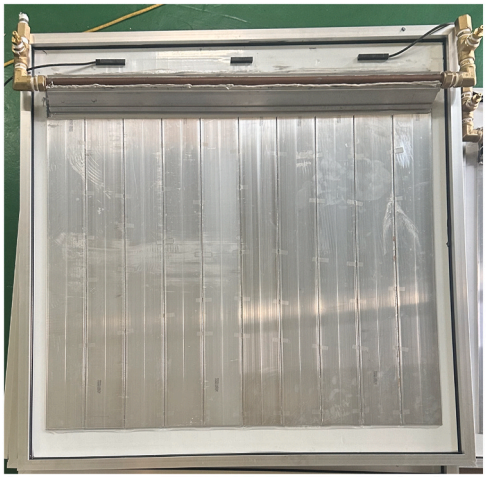

(c) Prototype panel rear view

(caption on next page)

Fig. 1. Overview of BIPVT module.

temperature variations [25]. Likewise, the Hottel–Whillier model, employed to predict thermal collection, cannot factor changes in thermal energy collection due to variations in the front-side cell temperature [26]. Therefore, this study proposes equations for predicting the electrical-power generation and thermal collection of BIPVT systems via estimation of the cell and outlet fluid temperatures on the basis of physical heat-transfer equations incorporating the associated heat-transfer mechanisms.

The models leveraged to calculate power generation are governed by apply a common fundamental equation for PV power output. Herein, the basic equation for the predicted power generation, P_{model}, is presented in Eq. (1).

$$P_{model} = I_v \times \eta_{ref} \times \left[1 + \beta \times \left(T_{cell} - T_{ref}\right)\right] \times A \times n \tag{1}$$

I_v is the vertical-plane solar irradiance (W/m^2), and η_{ref} is the reference electrical efficiency at the reference temperature T_{ref}. Herein, $\eta_{ref} = 0.159$ was adopted based on experimental results obtained conducted by a Korea laboratory accreditation scheme (KOLAS)-accredited international testing laboratory in Korea [12]. β denotes the temperature coefficient, reflecting the decrease in electrical efficiency with cell temperature increase, and a value of -0.0045/°C was adopted herein for this parameter [24]. T_{cell} denotes the cell temperature, and T_{ref} is the reference temperature, for which a value of 25 °C commonly considered for PV module performance comparison was adopted [27]. A is the area of a single module, which is 1 m^2, and n is the number of connected modules, which is 8. The equations utilized to calculate the predicted power generation P_{model} for each model and Eq. (1) are of the same form; however, they differ in terms of the method used to calculate T_{cell}.

The NOCT-based linear cell temperature model assumes that cell temperature increases linearly with solar irradiance, and it simplifies the actual heat transfer processes of the PV module [9,28]. The equation used to calculate $T_{cell,NOCT}$ in the NOCT-based linear cell temperature model is given in Eq. (2) [9].

$$T_{cell,NOCT} = T_{amb} + \frac{T_{NOCT} - 20}{800} \times I_v \tag{2}$$

where T_{amb} is the ambient air temperature. The NOCT represents the outdoor operating temperature of the module measured under the IEC 61215 test conditions namely, a solar irradiance of 800 W/m^2, ambient temperature of 20 °C, wind speed of 1 m/s, and natural ventilation and a value of 45 °C was adopted herein [29].

The Faiman model is a cell temperature prediction model based on the assumption that the temperature rise of a PV module increases with solar irradiance and decreases owing to wind. The thermal losses of the module are simplified into two components, namely, those due to natural and forced convection [22]. The equation used to calculate $T_{cell,Faiman}$ in the Faiman model is given in Eq. (3).

$$T_{cell,Faiman} = T_{amb} + \frac{I_v}{U_0 + U_1 \times v_{wind}} \tag{3}$$

Here, U_0 is the heat loss coefficient due to natural convection, U_1 is the forced convection heat loss coefficient associated with wind speed, and v_{wind} is the wind speed [22]. Herein, the measured wind speed data were not available. Therefore, representative coefficient values for crystalline silicon PV modules in mid-latitude regions commonly considered in PV performance modeling were adopted; i.e., $U_0 = 25.0$ W/(m^2·K) and $U_1 = 6.84$ W/(m^2·K·(m/s)) [22]. For models requiring wind speed as an input variable, a representative wind speed was assumed. From monthly average wind speed statistics provided by the Korea Meteorological Administration, indicating that

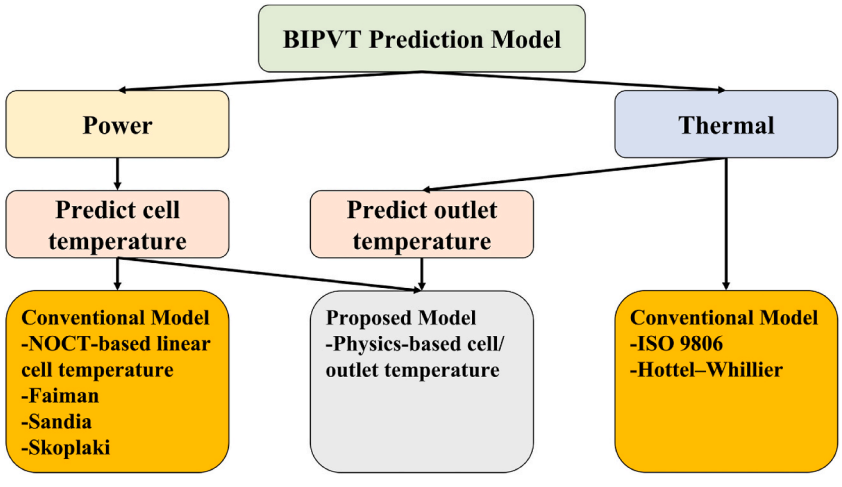

Fig. 2. Configuration of electrical and thermal prediction model.

the average wind speed in mid-latitude inland regions ranges from 1.7 to 2 m/s, a value of 2 m/s was adopted herein [30]. However, since these coefficient values are representative values derived under general PV module conditions, additional investigations are required in future studies for curtain wall-type BIPVT systems.

The SAPM model is an empirical cell temperature prediction model proposed by Sandia National Laboratories in the United States, incorporating cooling effects due to wind speed, solar irradiance, and module structural conditions in an exponential form. In this model, the cell temperature is calculated as the sum of the ambient air temperature and temperature rise, where the temperature rise is based on solar irradiance and wind speed [23]. Equations (4) and (5) are used to calculate $T_{cell,SAPM}$ in the SAPM model.

$$T_{cell,SAPM} = T_{SAPM} + \frac{I_V}{E_0}\Delta T_{SAPM} \tag{4}$$

$$T_{SAPM} = T_{amb} + I_v \times \exp\left(a + b \times v_{wind}\right) \tag{5}$$

Here, a represents the baseline temperature rise under low wind speed conditions and was fixed at -2.81 herein; b represents the cooling effect associated with increasing wind speed and was fixed at -0.0045/(m/s). E_0 is the reference irradiance used in the SAPM model and was fixed at 1000 W/m^2 [23]. The values of a and b were selected on the basis of the insulated-back module configuration representative coefficients provided in the Sandia module database [23], as no module-specific data dictionary was available for the BIPVT module employed herein. The coefficient b is required to be negative to ensure physical consistency; as the module temperature rises proportionally to irradiance and is attenuated by convective cooling, the exponential term $\exp\left(a + b \times v_{wind}\right)$ must decrease as wind speed increases to accurately represent the wind-driven cooling effect. A positive value of b would produce the physically incorrect result of increasing module temperature with increasing wind speed. Additionally, the cell-to-module temperature difference ΔT was fixed at zero, representing a conservative simplification in the absence of cell-level temperature measurement data. In this study, the SAPM coefficients a, b, and ΔT were set to the representative values provided in the insulated-back PV module database. This was because we were unable to obtain separate, experimentally measured calibration data for the liquid-cooled curtain-wall BIPVT structure, which was the subject of this study; therefore, these coefficients should be interpreted as first-order approximations for estimating cell temperature rather than optimized values for this specific system. Therefore, the SAPM results were used as a benchmark under the conditions of this study, and it will be necessary to recalibrate a, b, and ΔT using actual cell temperature data in the future.

The Skoplaki model extends the NOCT-based linear cell temperature empirical equation by incorporating the effect of wind speed on the temperature rise of PV modules. It features a corrected form of the NOCT model's temperature rise parameter, essentially adjusted using a convective heat transfer formulation to factor wind-induced cooling. The associated equations are Eq. (6) and Eq. (7) [24], where $h_{conv,ext}$ is the external convective heat transfer coefficient [31].

$$T_{cell,Skoplaki} = T_{amb} + \Delta T_{Skoplaki} \tag{6}$$

$$\Delta T_{Skoplaki} = \frac{T_{NOCT} - 20}{800} \times I_v \times \left(1 - \frac{\eta_{ref}}{\tau\alpha}\right) \times \frac{9.5}{h_{conv,ext}} \tag{7}$$

$$h_{conv,ext} = 5.7 + 3.8 \times v_{wind} \tag{8}$$

The transmittance τ was herein fixed at 0.96, representing the standard solar transmittance value for tempered glass covers widely adopted in PVT modeling. The absorptivity α was fixed at 0.9375, thereby yielding an effective transmittance–absorptance product of $\tau\alpha = 0.90$, which was consistent with the representative value for monocrystalline silicon cells referenced in the original Skoplaki formulation [24] and aligned with the Hottel–Whillier–Bliss collector theory framework.

Notably, both the SAPM and Skoplaki models involve a lumped-parameter approach wherein the cell temperature is represented as a single spatially averaged value for the entire module. Consequently, neither model explicitly resolves the spatial temperature distribution within the module such as the temperature gradient along the module height or local temperature variations at busbars, cell edges, and MFHP contact points. In the system proposed herein, the dominant source of spatial non-uniformity is the vertical thermal gradient arising from the upflow hydraulic configuration, wherein the fluid temperature increases from the bottom to the top of the array; the Skoplaki model implicitly factors the system-level effect of this gradient through the adoption of the representative ambient and inlet conditions. In terms of hotspots; those in standard PV modules typically arise from partial shading or cell-level electrical mismatch, leading to localized reverse-bias heating. In the BIPVT system proposed herein, the active liquid cooling afforded by the MFHP served as an inherent hot spot mitigation strategy, as continuous heat extraction reduces the steady-state temperature of all cells uniformly. Bypass diodes integrated into the module string provided additional protection against reverse-bias hotspot formation under partial-shading conditions. However, explicit hotspot modeling at the cell level exceeded the scope of this lumped-parameter simulation framework and is identified as a direction for future work involving spatially resolved thermal modeling.

The models employed calculate thermal energy collection are the ISO 9806 and Hottel–Whillier models. The ISO 9806 model is an energy balance-based model leveraged to predict the performance of flat-plate solar thermal collectors [14]. Equation (6) is used to calculate $Q_{ISO9806}$ in the ISO 9806 model.

$$Q_{ISO9806} = \left(\eta_0 \times I_v - a_1 \times \left(T_{in} - T_{amb}\right)\right) \times A \times n \tag{9}$$

Here, η_0 is the optical efficiency, representing the fraction of incident solar radiation absorbed as useful energy by the collector, and a_1

is the first-order heat loss coefficient, which linearly factors the reduction in useful energy due to thermal losses [32]. Both coefficients were measured herein via KOLAS-accredited performance testing, and the values of η_0 and a_1 were fixed at 0.2505 and 5.795 W/(m^2·K), respectively [12]. T_{in} denotes the inlet fluid temperature.

The Hottel–Whillier model is a physics-based thermal model originally developed for flat-plate solar collectors, enabling calculation of the useful thermal energy gain via balancing of absorbed solar radiation against thermal losses as a function of the fluid inlet temperature, ambient temperature, collector heat loss coefficient, and fluid flow rate [26]. Equations (10)–(12) used to calculate $Q_{Hottel-Whillier}$.

$$Q_{Hottel-Whillier} = F_R \times [I_v(\tau\alpha) - U_L \times (T_{in} - T_{amb})] \times A \times n \tag{10}$$

$$F_R = \frac{\dot{m} \times C_p}{A \times U_L} \times \left[1 - exp\left(\frac{-A \times U_L \times F'}{\dot{m} \times C_p}\right)\right] \tag{11}$$

$$F' = \frac{1}{U_L \times \left(\frac{1}{U_L} + \frac{1}{h_{conv,HW}} + R_{b\to tube}\right)} \tag{12}$$

Here, F_R is the heat removal factor reflecting the increase in useful thermal energy as heat is removed from the panel interior with increasing mass flow rate [33]. U_L is the overall heat loss coefficient of the collector (W/m^2·K), which quantifies the total rate of thermal losses from the collector surface to the surrounding environment per unit area and per unit temperature difference. Herein, U_L was adopted as equal to the first-order heat loss coefficient a_1, as defined in ISO 9806 [14], which represented the linear (temperature-independent) component of the total heat loss. Given the vertically mounted, unglazed rear-surface BIPVT curtain wall configuration wherein the exterior glass surface is directly exposed to ambient convection and radiation with reduced wind exposure compared to roof-mounted systems, a value of a_1 in the range of 5–8 W/(m^2·K) was physically consistent with the thermal loss characteristics of comparable unglazed vertical BIPVT systems [14]. $\dot{m}$ is the mass flow rate of the heat transfer fluid, and C_p is the specific heat capacity of the fluid. Herein, antifreeze was utilized to prevent freezing during winter operations; therefore, C_p was fixed at 3750 J/(kg·K), and a density value of 1040 kg/m^3 was adopted for calculating the mass flow rate $\dot{m}$ [34]. F' represents the effective heat transfer capability between the collector and heat transfer fluid. $h_{conv,HW}$ is the internal convective heat transfer coefficient between the copper tube and heat transfer fluid; as opposed to detailed calculations, a representative value of 800 W/(m^2·K) for turbulent flow was adopted in the Hottel–Whillier model. Finally, $R_{b\to tube}$ denotes the thermal resistance between the rear side of the module and the copper tube.

In addition to the four power generation prediction models and two thermal collection prediction models introduced earlier, this study presents a physics-based cell and outlet temperature prediction model incorporating heat-transfer mechanisms and proposes a model capable of simultaneously calculating power generation and thermal collection.

The proposed cell/outlet fluid temperature prediction model is a numerical model enabling cell temperature $T_{cell,physics}$ prediction by factoring heat transfer through the thermal resistances of each layer based on the multilayer conduction structure of the BIPVT module; the power generation can also be calculated accordingly. The outlet fluid temperature $T_{out,physics}$ can be predicted via an energy conservation equation that considers heat exchange between the copper tube and heat-transfer fluid, and thermal energy collection can then be calculated. The overall calculation procedure associated with the model is as follows.

$$T_{cell,physics} = T_f - (T_f - T_b) \times \frac{R_{f\to cell}}{R_{total}} \tag{13}$$

Here, T_f is the front surface temperature, determined using a front-side energy balance equation under the assumption that absorbed solar energy at the module front surface is balanced by radiative and convective losses to the sky and ambient air [33].

$$\alpha \times I_v = \varepsilon \times \sigma \times \left[(T_f + 273.15)^4 - (T_{sky} + 273.15)^4\right] + h_{conv,ext} \times (T_f - T_{amb}) \tag{14}$$

Here, ε is the front surface emissivity, fixed at 0.85, and σ is the Stefan–Boltzmann constant, fixed at 5.67×10^{-8} W/(m^2·K^4) [31]. T_{sky} is the sky radiation temperature, defined by an empirical equation based on ambient air temperature, and it was calculated using Eq. (15).

$$T_{sky} = 0.0552(T_{amb} + 273.15)^{1.5} - 273.15 \tag{15}$$

T_b is the rear surface temperature. Assuming a balance between that the conductive heat transfer from the front surface to the rear surface with heat losses at the rear surface, the thermal resistance–based relationship is expressed by Eq. (16) [35].

$$\frac{T_f - T_b}{R_{total}} \times A = \frac{T_b - T_{amb}}{R_{back,total}} \times A \tag{16}$$

Herein, because an air layer existed between the building wall and the BIPVT, the ambient air temperature was adopted as an approximation. $R_{f\to cell}$ is the thermal resistance from the front surface to the cell, R_{total} is the total thermal resistance of all the layers, and $R_{back,total}$ is the thermal resistance of the rear side layer including insulation. The nonlinear energy balance equations determining

T_f and T_b were numerically solved using the Newton–Raphson iterative method to obtain the front and rear surface temperatures, from which the cell temperature was predicted [36].

From the calculated front and rear surface temperatures, the outlet fluid temperature was predicted by assuming that the conductive heat transferred from the rear surface to the copper tube is balanced by the sum of heat losses from the tube to the ambient air and heat transferred to the heat transfer fluid. The copper tube temperature T_{tube} was numerically solved using the Newton–Raphson iterative method, as shown in Eq. (17) [36].

$$\frac{T_b - T_{tube}}{R_{b\to tube}} \times A_{pipe} = \frac{T_{tube} - T_{amb}}{R_{back,total}} \times \left(A_{pipe,hex} + A_{pipe,con}\right) + h_{conv,fluid} \times \left(T_{tube} - T_{in}\right) \times A_{pipe} \tag{17}$$

Here, A_{pipe} is the effective heat transfer area directly involved in the heat exchange between the copper tube and the heat transfer fluid inside the module. $A_{pipe,hex}$ and $A_{pipe,con}$ are the areas of the copper tube exposed to heat exchange with the ambient air in the module passage section and the module connection section, respectively. Heat is gained in the module passage section, while heat is lost in the module connection section. $h_{conv,fluid}$ is the internal convective heat transfer coefficient inside the tube. Herein, it was calculated using the Dittus–Boelter correlation, as shown in Eqs. (18)–(21) [37].

$$h_{conv,fluid} = \frac{Nu \times k}{D} \tag{18}$$

$$Nu = 0.023 Re^{0.8} \times Pr^{0.4} \tag{19}$$

$$Re = \frac{4\dot{m}}{\pi D \mu} \tag{20}$$

$$Pr = \frac{\mu \times C_p}{k} \tag{21}$$

Here, Nu is the Nusselt number, k is the thermal conductivity of the heat transfer fluid, fixed at 0.4 W/(m·K), and D is the tube diameter, fixed at 0.0222 m Re is the Reynolds number, and Pr is the Prandtl number, representing the ratio of momentum diffusivity to thermal diffusivity. The viscosity of the heat transfer fluid, μ, was fixed at 0.0035 [38]. Subsequently, the predicted outlet fluid temperature $T_{out,physics}$ was calculated using the energy conservation equation given in Eq. (22).

$$T_{out,physics} = T_{in} + \frac{h_{conv,fluid} \times \left(T_{tube} - T_{in}\right) \times A_{pipe}}{\dot{m} \times C_p} \tag{22}$$

The predicted thermal energy collection $Q_{physics}$ was calculated from the predicted outlet temperature using Eq. (23).

$$Q_{physics} = \dot{m} \times C_p \times \left(T_{out,physics} - T_{in}\right) \tag{23}$$

The thermal resistance values R_i adopted in the calculation of power generation and thermal collection in the physics-based cell/outlet fluid temperature prediction model utilizing heat-transfer mechanisms were determined using Table 1 and Eq. (24). The layer structure of the module is shown in Fig. 1(a), and the area of one module was 1×1 m^2. The layers comprised glass, an EVA film, a solar cell, EVA film, heat pipe, thermal compound, manifold, copper tube, and EPDM. The material properties of each layer are listed in Table 1.

Accordingly, the thermal resistance R_i was calculated using Eq. (24).

$$R_i = \frac{L_i}{k_i} \tag{24}$$

Here, L_i is the thickness of the corresponding layer and k_i is the thermal conductivity of that layer.

Herein, simulations were conducted under identical operating conditions using the four power generation prediction models and two thermal collection prediction models defined above, along with the physics-based cell/outlet fluid temperature prediction model

Table 1
Material properties of BIPVT module layers.

Layer	Thickness [mm]	Conductivity [W/(m•K)]
Glass	5	1.5
EVA film2	0.5	0.3
Solar cell	0.2	148
EVA film1	0.5	0.3
Heat pipe	1.5	237
Thermal compound	0.5	9.1
Manifold	2.5	237
Copper tube	22.2(ϕ)	401
EPDM insulation	20	0.13

capable of simultaneously predicting power generation and thermal collection. The prediction accuracy of each model was then evaluated via comparisons with the measured data.

3. Experiment

3.1. Experimental setup

The experiment was conducted on eight BIPVT modules installed on the south-facing envelope of the energy-plus solar house (KePSH-2) building at the Zero Energy Performance Test Building of the Korea Institute of Energy Research, located in Daejeon, Republic of Korea. The experimental period spanned from 1 September 2025 to 8 November 2025, during which the BIPVT system was operated continuously except for several excluded days, and power generation and thermal collection data were measured. Fig. 3 depicts the BIPVT modules installed on the KePSH-2 building.

On the basis of this structure, the BIPVT system was designed as a multi-heat-source integrated system capable of utilizing both solar thermal and geothermal energy. Fig. 4(a) presents a conceptual diagram of the overall operating system, comprising the BIPVT system, a thermal storage tank, a ground heat exchanger, and a water-source heat pump. Solar thermal energy recovered from the BIPVT was transferred to the thermal storage tank through a heat exchanger and stored, and the stored heat was utilized as a heat source for the water-source heat pump, depending on the operating conditions. The ground heat exchanger operated as an auxiliary heat source supplying heat to the water-source heat pump, depending on ground temperature, thereby ensuring heat source stability of the system even under conditions wherein solar thermal utilization was limited.

The BIPVT module featured a multilayer structure, wherein tempered glass and PV cells for solar power generation were located on the exterior side, whereas heat pipes and fluid flow channels for solar thermal collection were arranged on the interior side. The arrangement of measurement sensors and flow channels is shown in Fig. 4(b).

The measured data included vertical-plane solar irradiance I_v, ambient air temperature T_{amb}, inlet fluid temperature T_{in} , outlet fluid temperature T_{out}, volume flow rate V, and measured power generation $P_{measured}$. The solar irradiance and ambient air temperature were measured in units of W/m^2 and °C, respectively, using a pyranometer and thermometer installed on the rooftop of the KePSH-2 building. As shown in Fig. 4, resistance temperature detectors (RTDs) are installed on the inlet and outlet pipes to respectively measure the inlet and outlet fluid temperatures in units of °C, and a flow meter is installed on the outlet pipe to measure the flow rate of the heat transfer fluid in units of L/min. The experimental procedure was as follows. At the start of each operating day, the circulation pump was activated when the measured vertical-plane solar irradiance exceeded 50 W/m^2, at which point the heat transfer fluid began circulating through the BIPVT modules, heat exchanger, and thermal storage tank. The volume flow rate was maintained at a constant set-point of 8–18 L/min, controlled automatically by the programmable logic controller (PLC)-based system. This range reflects the actual operating conditions during the experiment rather than a separate flow rate parameter sweep; the system was operated primarily in the 8–10 L/min range during the early part of the experiment and in the 16–18 L/min range during the latter part. Data acquisition commenced simultaneously with pump activation and proceeded until irradiance fell below the activation threshold or until the end of the day. Days were excluded from the analysis if instrument malfunction, pump downtime, or irradiance below the minimum threshold persisted for more than 1 h of the potential operating window.

In the context of sensor placement, two RTDs (accuracy of ±0.2 °C) were installed in the hydraulic loop to measure the system-level fluid temperatures Tin and Tout. The inlet RTD was installed on the supply pipe immediately upstream of the BIPVT module inlet, whereas the outlet RTD was installed on the return pipe approximately 18 m downstream after the fluid had passed through the BIPVT modules. Notably, individual per-module temperature sensors were not installed; therefore, the present measurements represent system-level thermal conditions rather than module-level or cell-level temperature distributions. In this study, the inlet and outlet temperature sensors were installed approximately 18 m away from the BIPVT array; consequently, the measured fluid temperatures



Fig. 3. BIPVT curtain-wall installation on KePSH-2 building.

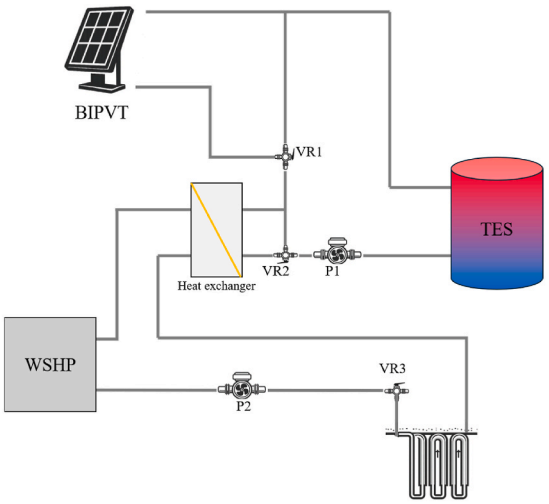

(a) BIPVT operating system

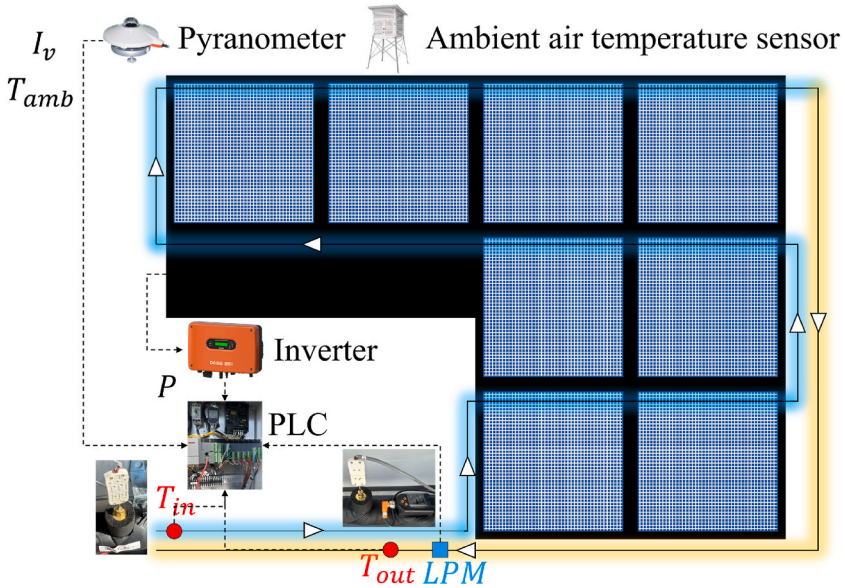

(b) Hydraulic loop and sensor layout of the BIPVT system

Fig. 4. BIPVT system overview.

may reflect heat loss occurring in the piping section. However, the physics-based model used in this study was constructed by distinguishing between heat gain and heat loss sections based on length, and the piping sections where heat loss could occur were insulated with EPDM insulation to minimize additional heat loss. Therefore, the outlet water temperature measured in this study is interpreted as a value representing the average fluid temperature at the system level rather than the local outlet temperature of a single module. The solar irradiance I_v was measured using a first-class pyranometer mounted on the rooftop of the KePSH-2 building at an elevation consistent with that of the BIPVT array, and the ambient temperature T_{amb} was measured using a mechanically aspirated thermometer at the same location. All data were recorded at 1-min intervals using a PLC-based data acquisition system.

3.2. Uncertainty analysis

Herein, an uncertainty analysis of the measured input variables was conducted to ensure the reliability of the experimental results. The uncertainty evaluation was performed as per the method proposed by Kline and McClintock (1953), wherein Type An uncertainty arising from repeated measurements and Type B uncertainty based on instrument specifications were first estimated; and then

combined to calculate the total uncertainty [39].

For each measured variable x, the mean value $\overline{x}$ and standard deviation σ_x were calculated from N data points, and the relative Type An uncertainty $\delta_{vr,x}$ was defined as expressed in Eq. (25) [39].

$$\delta_{vr,x} = \frac{\sigma_x}{\sqrt{N}\overline{x}} \times 100 \tag{25}$$

The Type B uncertainty $\delta_{ve,x}$ was determined from the accuracy specifications of the sensors and measurement instruments. The relative combined uncertainty $\delta_{v,x}$ of each measured variable x was then calculated by combining the Type A and Type B uncertainties using the root-sum-square method, as shown in Eq. (26) [39]. The results are presented in Table 2.

$$\delta_{v,x} = \sqrt{\left(\delta_{vr,x}\right)^2 + \left(\delta_{ve,x}\right)^2} \tag{26}$$

4. Results

4.1. Experimental results for BIPVT system

Fig. 5 shows the variations in vertical-plane solar irradiance I_v and ambient air temperature T_{amb}. On clear days in September, the vertical-plane solar irradiance increased to 801 W/m^2, and the daytime ambient air temperature ranged from 18.6 to 35.4 °C. As the experiment progressed into November, the duration of sunshine and solar altitude decreased; however, the daily maximum solar irradiance increased up to 959 W/m^2, increasing vertical-plane solar irradiance, whereas the ambient air temperature decreased to an average of 11.2 °C.

Fig. 6 presents the variations in inlet temperature T_{in} , outlet temperature T_{out}, and flow rate V from 6:00 a.m. to 6:00 p.m. for three selected days during the experimental period. As shown, the inlet temperature generally follows the trend of ground temperature; during periods when the pump is in use, and the flow rate is maintained, the outlet temperature is approximately 0.0–5.0 °C higher than the inlet temperature. Moreover, the flow rate is maintained within the range of 0.0–19.9 L/min. The lower subplot of each panel shows the temperature difference ΔT, denoting the active heat recovery periods when the pump is in operation and thermal energy is being extracted.

With regard to Fig. 6(a) and (b), the flow rate is maintained within the range of 8.3–12.7 L/min, the inlet temperature ranges from 20.5 to 40.5 °C, and the outlet temperature ranges from 23.2 to 40.7 °C. Moreover, the average temperature difference between the inlet and outlet during pump operation is 1.3 °C. With regard to Fig. 6(c)–(f), the flow rate and inlet/outlet temperatures during operation exhibit periodic fluctuations. This behavior is interpreted as having been caused by heat exchange with the ground-side heat exchanger during operation, as the system is configured to exchange heat with the ground, as shown in Fig. 4(a). As shown in Fig. 6(c) and (d), the inlet temperature ranges from 20.4 to 40.9 °C, and the outlet temperature ranges from 19.8 to 41.4 °C, with an average inlet–outlet temperature difference of 0.9 °C during pump operation. As shown in Fig. 6(e) and (f), the inlet temperature ranges from 22.6 to 41.2 °C, and the outlet temperature ranges from 21.7 to 41.7 °C, with an average inlet–outlet temperature difference of 0.6 °C during pump operation. Prior to pump startup, ΔT remained near-zero or slightly negative, as no fluid circulation occurred. Once the pump commenced operating, ΔT increased to positive values, with average values of 1.3, 0.9, and 0.8 °C for September, October, and November, respectively. Peak values of 7.7, 11.9, and 7.9 °C were observed during periods of high solar irradiance in each respective month.

Fig. 7 shows the daily cumulative energy collection of the instantaneous electrical power $P_{measured}$ measured at the inverter and the thermal energy collection $Q_{measured}$ calculated from the temperature and flow rate measurements. On clear days, the maximum instantaneous electrical power reached approximately 1100 W, and the maximum instantaneous thermal energy collection reached up to 9049.8 W. Daily, the power generation ranged from 0.0 to 6.2 kWh/day, and the thermal energy collection ranged from 0.0 to 9.5 kWh/day.

The power generation efficiency η_{el} and thermal energy collection efficiency η_{th} were calculated using Eq. (25) and Eq. (26); respectively, from the measured data.

$$\eta_{el} = \frac{P_{measured}}{I_v \times A \times n} \times 100 \tag{27}$$

Table 2
Results pertaining to uncertainty.

Variable	N	Mean	Type A	Type B	Combined	Unit
I_v	55,257	511.458	0.418	4.000	4.022	%
T_{amb}	55,257	19.277	0.069	0.189	0.201	°C
T_{in}	55,257	32.077	0.049	0.214	0.220	°C
T_{out}	55,257	32.656	0.049	0.216	0.221	°C
V	55,257	15.378	0.148	3.000	3.005	%
$P_{measured}$	55,257	0.447	0.643	2.000	2.101	%

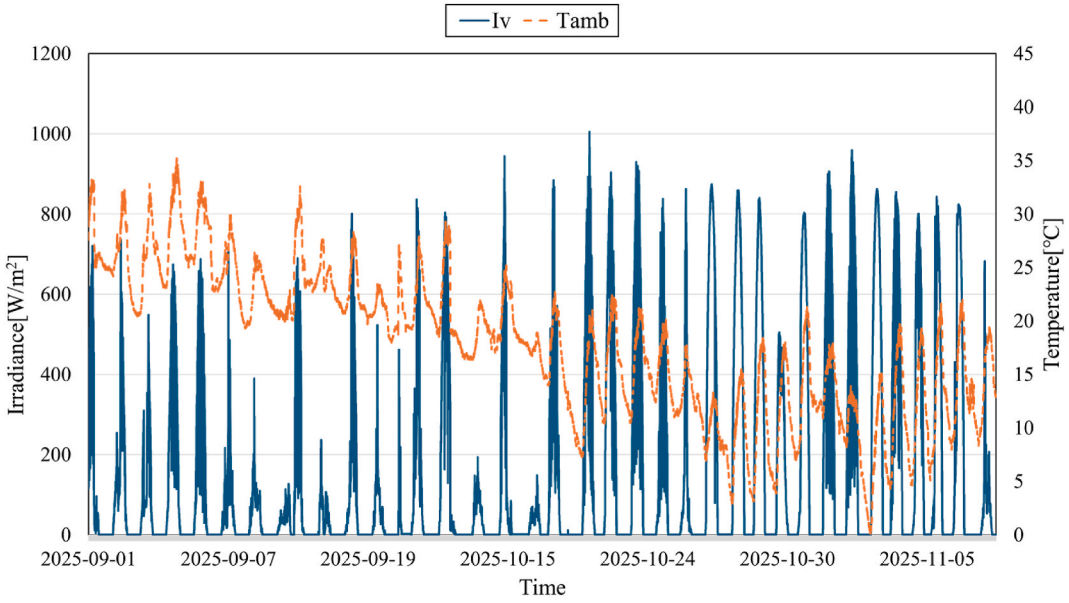

Fig. 5. Measured vertical irradiance and ambient air temperature.

$$\eta_{th} = \frac{\dot{m} \times C_p \times (T_{out} - T_{in})}{I_v \times A \times n} \times 100 \tag{28}$$

Here, $P_{measured}$ is the measured electrical power generation recorded by the inverter (W). The numerator of Eq. (26), $\dot{m} \times C_p \times (T_{out} - T_{in})$, represents the measured useful thermal energy gain derived from the temperature difference between the manifold outlet and inlet. The common denominator represents the total solar energy incident on the entire BIPVT array (W). Fig. 8 presents the power generation efficiency and thermal collection efficiency calculated from the measured solar irradiance, power generation, and thermal energy collection. The total solar irradiance in September was 180.5 kWh, with a power generation efficiency of 7.1% and a thermal energy collection efficiency of 17.6%. In October, the total solar irradiance was 565.7 kWh, and the power generation efficiency and thermal energy collection efficiency were 8.2% and 9.6%, respectively. In November, the total solar irradiance was 310.5 kWh, with a power generation efficiency of 9.2% and a thermal energy collection efficiency of 10.9%. The efficiencies are presented herein as system efficiencies, calculated as the sum of the power generation and thermal energy collection during periods with solar irradiance.

Additionally, to examine the heat exchange characteristics across different flow rate ranges within the actual operating range of this study, a comparison graph with solar irradiance on the x-axis and thermal efficiency and heat collection rate on the y-axis was added in Fig. 9. The comparison results showed that in the 8–10 L/min range, an average solar irradiance of 301.5 W/m^2 yielded an average thermal efficiency of 17.4% and and an average heat collection capacity of 0.50 kW; the 16–18 L/min range showed an average thermal efficiency of 11.1% and an average heat collection capacity of 0.64 kW at an average solar irradiance of 562.8 W/m^2. In other words, while the average heat collection rate increased by approximately 28% in the high-flow-rate range, the average thermal efficiency was approximately 6.3 percentage points lower due to the denominator effect caused by the increase in solar irradiance. However, both ranges exhibited the same trend of increasing heat collection rate with increasing solar irradiance, confirming that, within the actual operating range of this study, although changes in flow rate may affect the absolute values of heat exchange performance, the overall trend remains consistent.

4.2. Simulation results

4.2.1. Cell temperature

Herein, because the cell temperature of the module could not be directly measured during the experimental period, the cell temperatures predicted by the models employed for power-generation prediction were compared and analyzed for each model. Fig. 10 shows the cell temperatures predicted by each power generation prediction model. All the models exhibited a diurnal pattern, wherein cell temperature increased from the morning with increasing solar irradiance, reached a maximum around noon, and then decreased.

Fig. 10(a) shows the cell temperature variation for a single day during the entire period. On that day, the maximum cell temperatures were estimated to be 39.5 °C for the NOCT model, 55.4 °C for the Faiman model, 59.5 °C for the SAPM model, 28.9 °C for the Skoplaki model, and 41.5 °C for the physics-based model, with noticeable differences indicated among the models in the peak period. By contrast, the minimum cell temperatures were estimated as 0.1 °C for the NOCT, Faiman, SAPM, and Skoplaki models, and 1.4 °C for the physics-based model, confirming the stronger cooling effects during nighttime and low-irradiance periods for the physics-based model. The daily average cell temperatures over the entire period were estimated to be 24.8 °C for the NOCT model, 34.3 °C for the

Faiman model, 36.8 °C for the SAPM model, 18.4 °C for the Skoplaki model, and 28.1 °C for the physics-based model. As the experiment progressed from September to November, the peak cell temperatures gradually decreased.

The monthly cell temperature distribution results showed that The monthly median values generally decreased from September to October, while the November median slightly rebounded for some models. Specifically, NOCT and Skoplaki showed lower medians in October and remained similar or slightly higher in November, whereas Faiman, Sandia, and the physics-based model showed an increasing tendency from September to November. Moreover, the distribution range tended to widen over time. Particularly, the physics-based model showed an extension as low as 2.3 °C in October and 0.3 °C in November, indicating that it reflected the lower thermal response during low-irradiance periods. By contrast, the Faiman and SAPM models showed nearly similar monthly median values and distribution ranges, and the Skoplaki model generally predicted relatively lower cell temperatures overall.

In Fig. 10(d)–a wind speed sensitivity analysis was performed to determine how sensitive the cell temperature predictions of the Faiman, SAPM, and Skoplaki models which directly use wind speed inputs are to changes in wind speed. Since no actual on-site wind speed measurements were available for this study, the monthly average wind speed of 2.0 m/s from a weather station was used as the reference value, and the wind speed was varied in the range of 0.0 to 3.0 m/s in 0.5 m/s increments. As a result, the deviation in average cell temperature ranged from 37.3 °C to 29.5 °C for the Faiman model, from 46.0 °C to 42.7 °C for the SAPM model, and from 38.8 °C to 26.3 °C for the Skoplaki model. Although an increase in wind speed tended to lower the cell temperature in all three models,

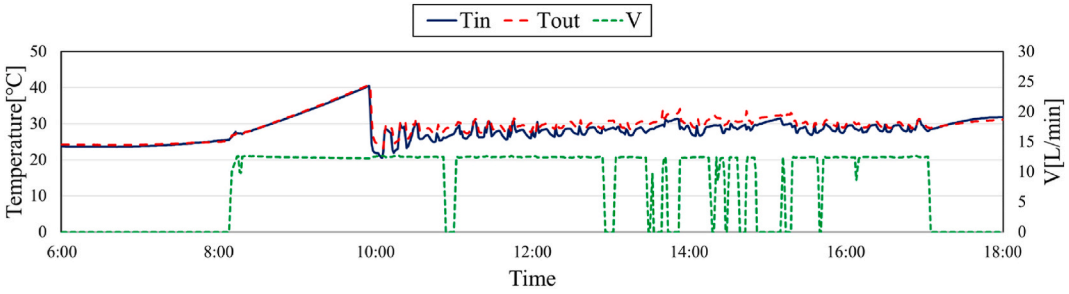

(a) Temperature and flow rates on 2025-09-05

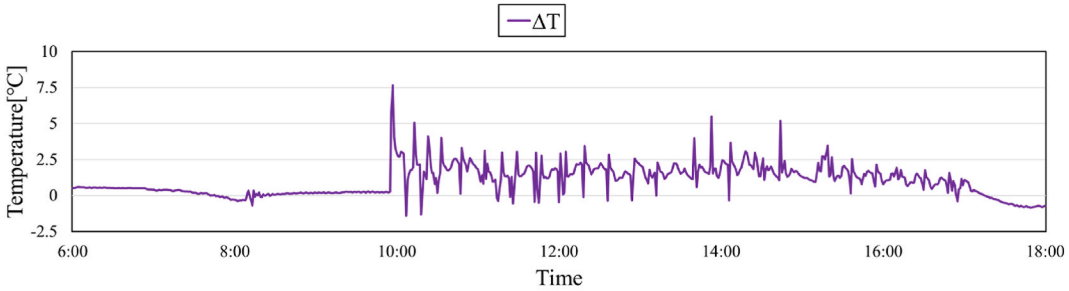

(b) Temperature difference on 2025-09-05

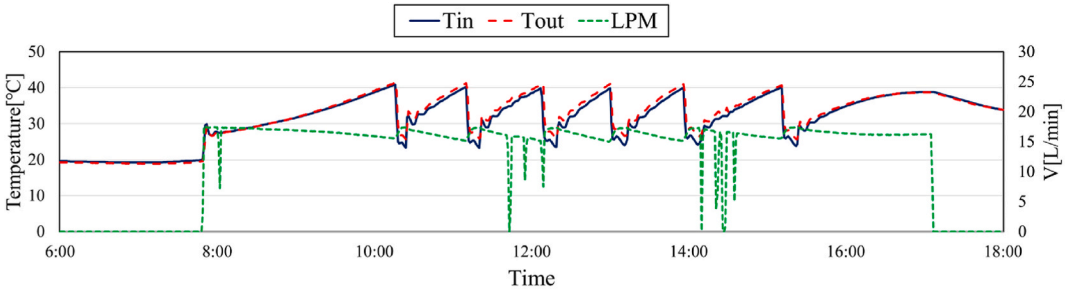

(c) Temperature and flow rates on 2025-10-11

Fig. 6. Measured time series data on representative days

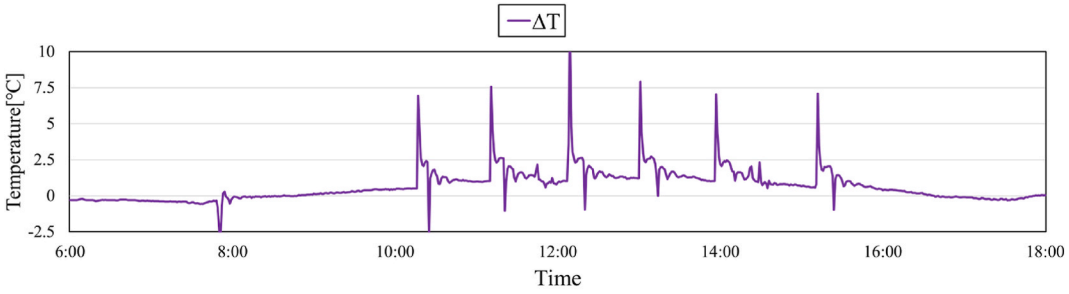

(d) Temperature difference on 2025-10-11

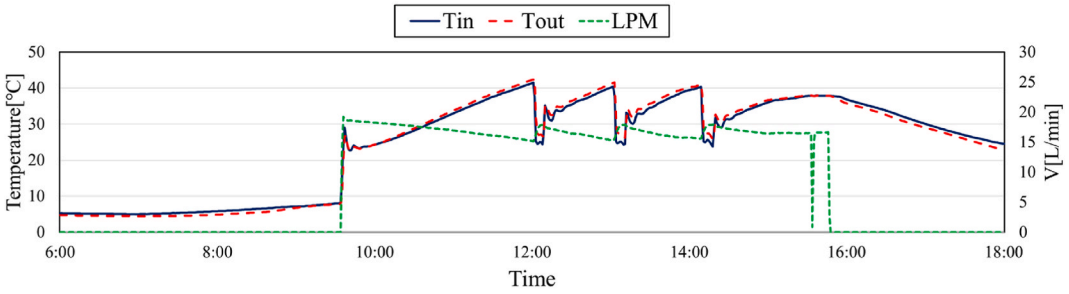

(e) Temperature and flow rates on 2025-11-05

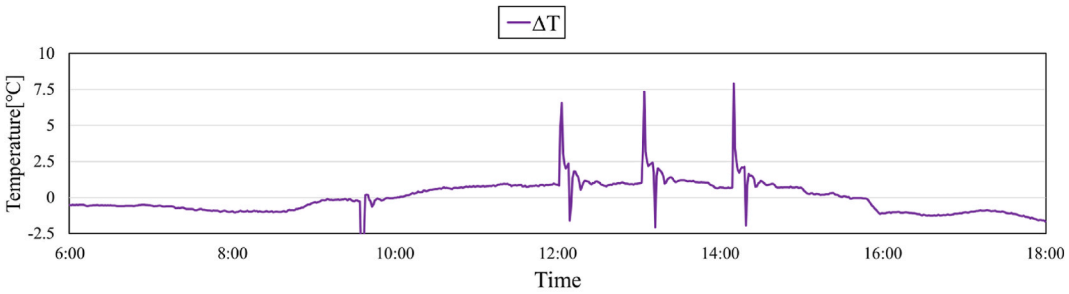

(f) Temperature difference on 2025-11-05

Fig. 6. (*continued*).

the impact on power generation was deemed to be relatively minor; therefore, the monthly average wind speed of 2.0 m/s was used in the analysis.

4.2.2. Outlet fluid temperature

Herein, several thermal collection models were applied to predict the thermal performance. Among them, only the physics-based model enables the direct calculation of the predicted outlet fluid temperature using heat balance equations incorporating a multilayer thermal resistance structure and convective heat transfer between the copper tube and the fluid. By contrast, the ISO 9806 and Hottel–Whillier models are performance-based models for calculating the useful thermal energy and cannot be used to compute outlet fluid temperature. Therefore, for the 9806 and Hottel–Whillier models, the outlet fluid temperature was back-calculated using the calculated thermal collection along with the measured inlet temperature and flow rate, and then compared with the measured outlet temperature, whereas the outlet temperature predicted using the physics-based model was directly compared.

Fig. 11 presents the inlet and outlet temperatures, predicted and back-calculated outlet temperatures, and flow rate. Fig. 11(a) corresponds to 3 November, as also shown in Fig. 6, and exhibits a pattern of increasing and decreasing temperatures following changes in flow rate. The predicted and back-calculated outlet temperatures were not available for some periods. These correspond to periods when the flow rate was zero; because the flow rate was an input variable in the prediction and back-calculation processes, the

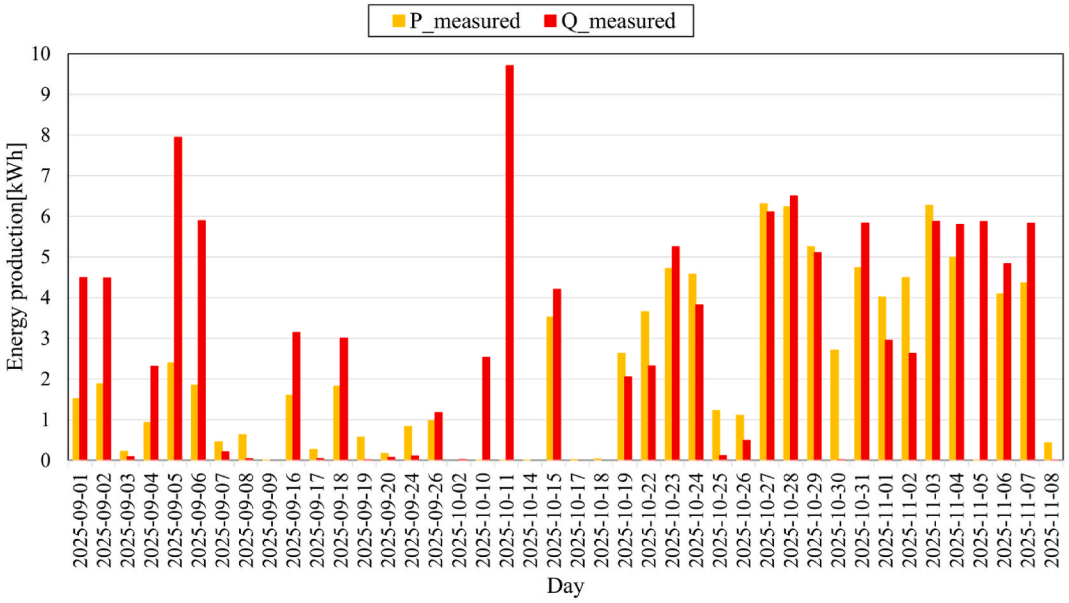

Fig. 7. Daily measured power generation and thermal energy collection.

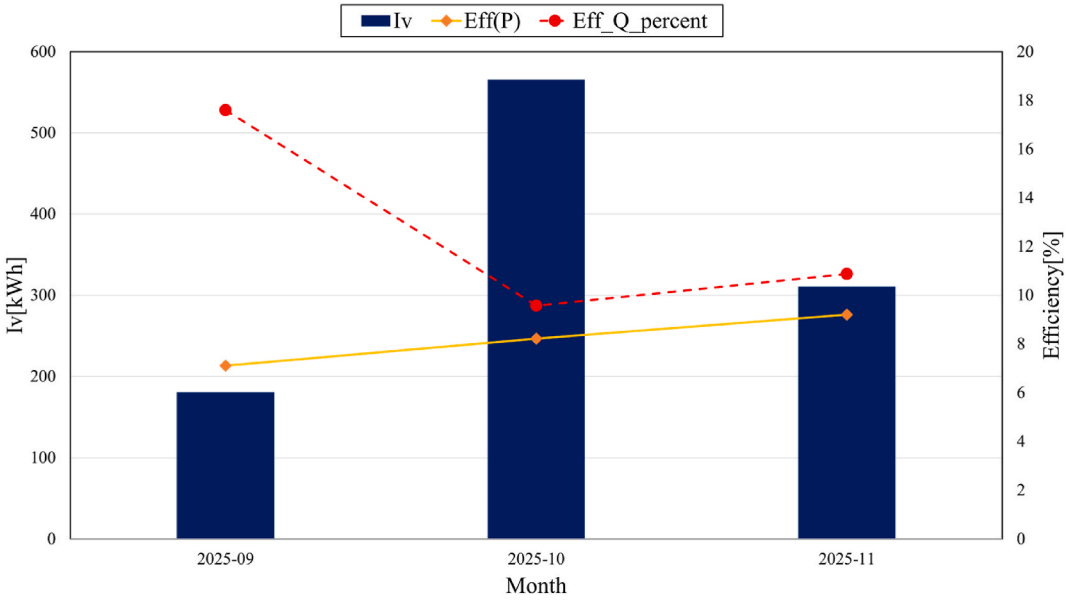

Fig. 8. Power generation and thermal energy collection efficiency.

predicted and back-calculated outlet temperatures were not calculated during pump shutdown periods.

On that day, the measured outlet temperature averaged at 34.6 °C, and the physics-based model predicted an average outlet temperature of 34.5 °C, showing close agreement. The maximum outlet temperature was 41.7 °C in the measurements, and the physics-based model predicted a value of 41.6 °C, also closely matching the peak value. By contrast, the ISO 9806 model predicted an average outlet temperature of 34.1 °C and a peak of 41.4 °C, and the Hottel–Whillier model predicted an average of 35.1 °C and a peak of 42.2 °C; the differences from the measured values were small, and both models predicted values within a range close to the measurements.

The monthly outlet temperature distribution results show that the monthly median of the measured outlet temperature was 30.0 °C in September, 34.1 °C in October, and 34.5 °C in November. For the ISO 9806 model, the monthly medians were 30.1 °C in September, 34.1 °C in October, and 33.8 °C in November; and the Hottel–Whillier model predicted 31.7 °C in September, 34.6 °C in October, and 34.3 °C in November. The physics-based model predicted 30.1 °C in September, 33.5 °C in October, and 34.5 °C in November. The

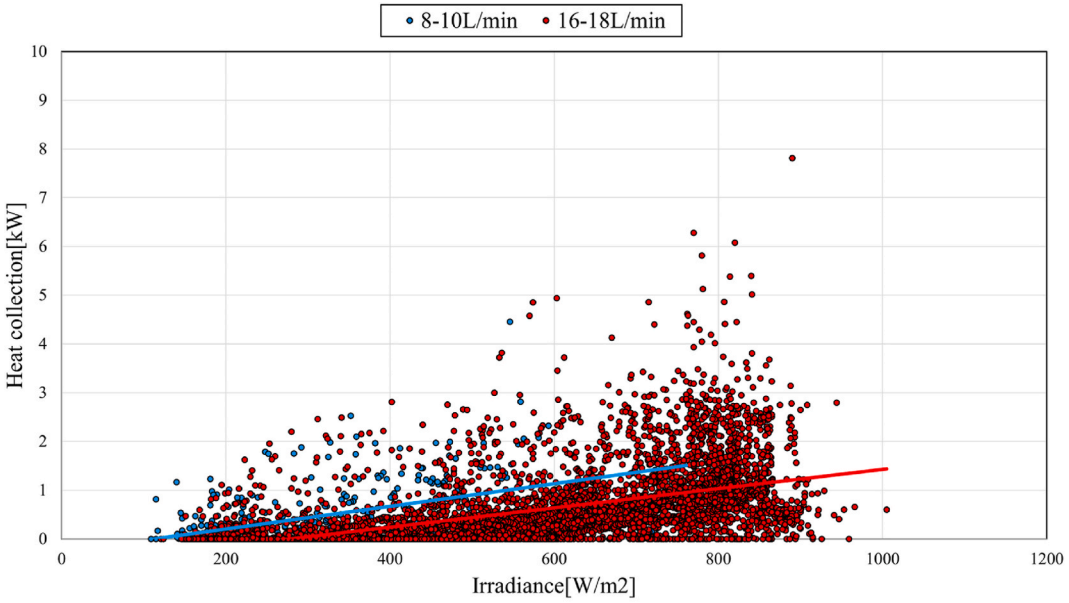

(a) Irradiance versus heat collection

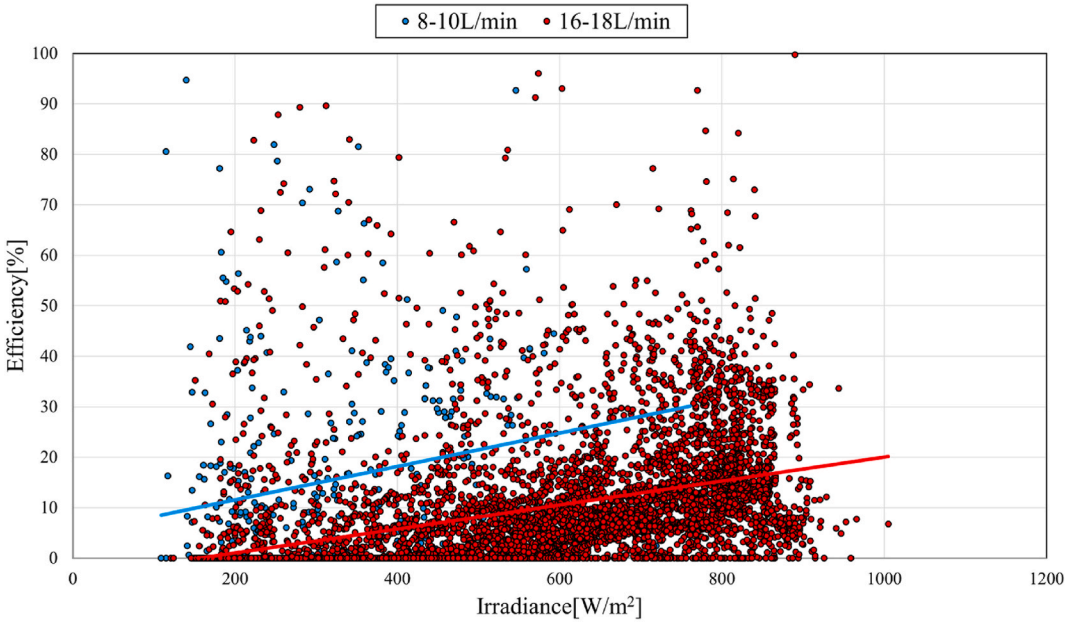

(b) Irradiance versus efficiency

Fig. 9. Comparison of thermal efficiency and heat collection according to flow-rate bands.

measured outlet temperature and the physics-based model showed similar behavior not only in terms of monthly median values but also in distribution range, whereas the ISO 9806 and Hottel–Whillier models exhibited closely matched predictions to each other in both distribution range and variability.

4.3. Validation results

Herein, the four aforementioned power generation prediction models and two thermal energy collection prediction models, along with one model capable of simultaneously predicting power generation and thermal energy collection, were proposed and validated through comparisons with measured power generation and thermal energy collection data. The simulation results were comparatively validated using monthly cumulative power generation and thermal energy collection, as well as total cumulative power generation and thermal energy collection over the entire period, on the basis of the RMSE and error rate. Moreover, the measured outlet temperature

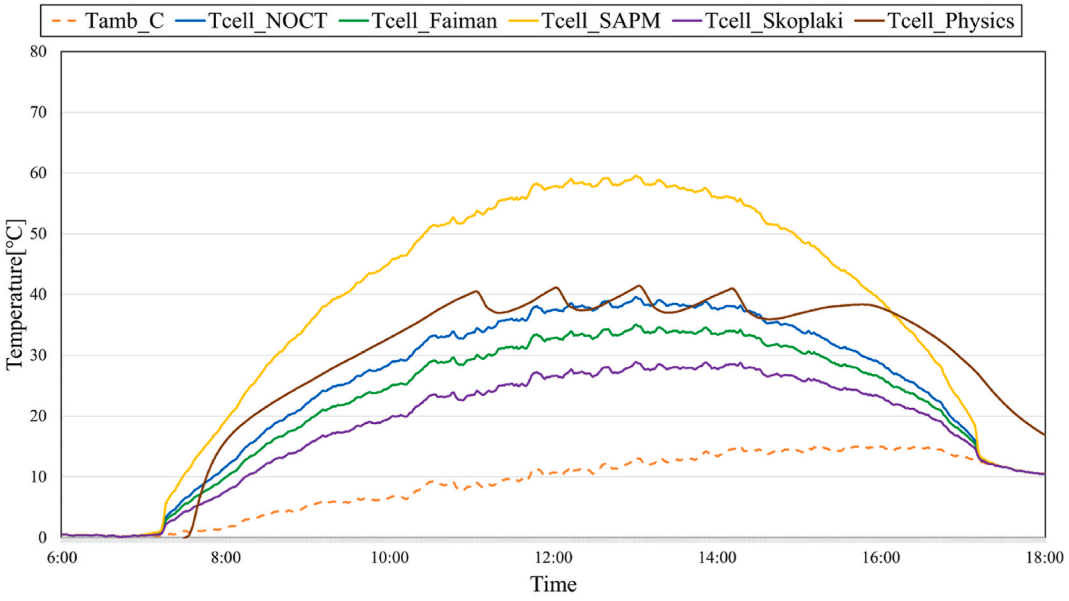

(a) Minute-resolution cell temperature profile

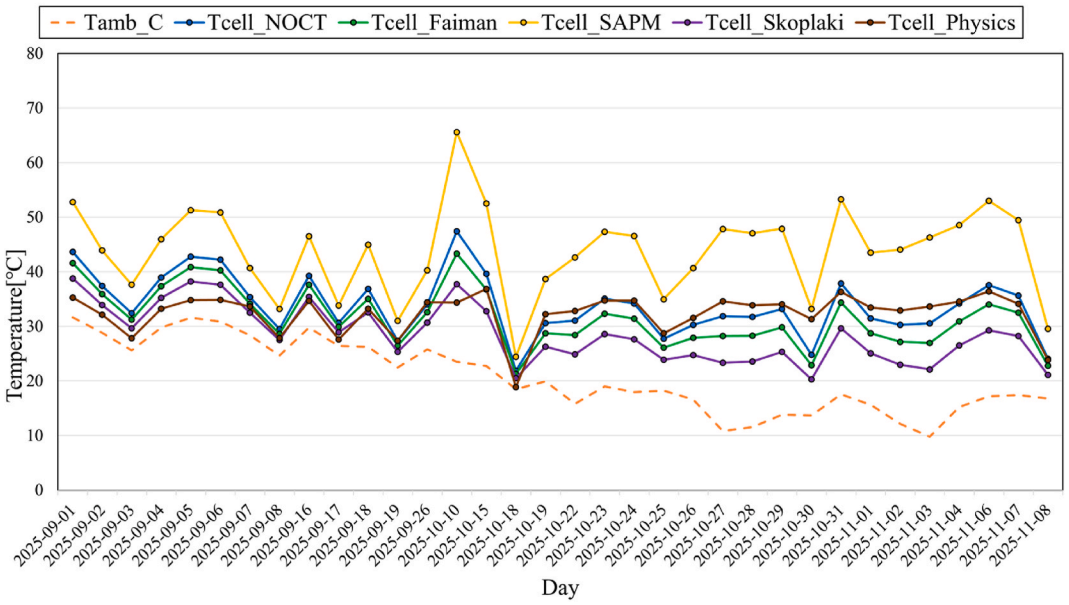

(b) Daily averaged cell temperature

Fig. 10. Cell temperature of each power generation prediction model.

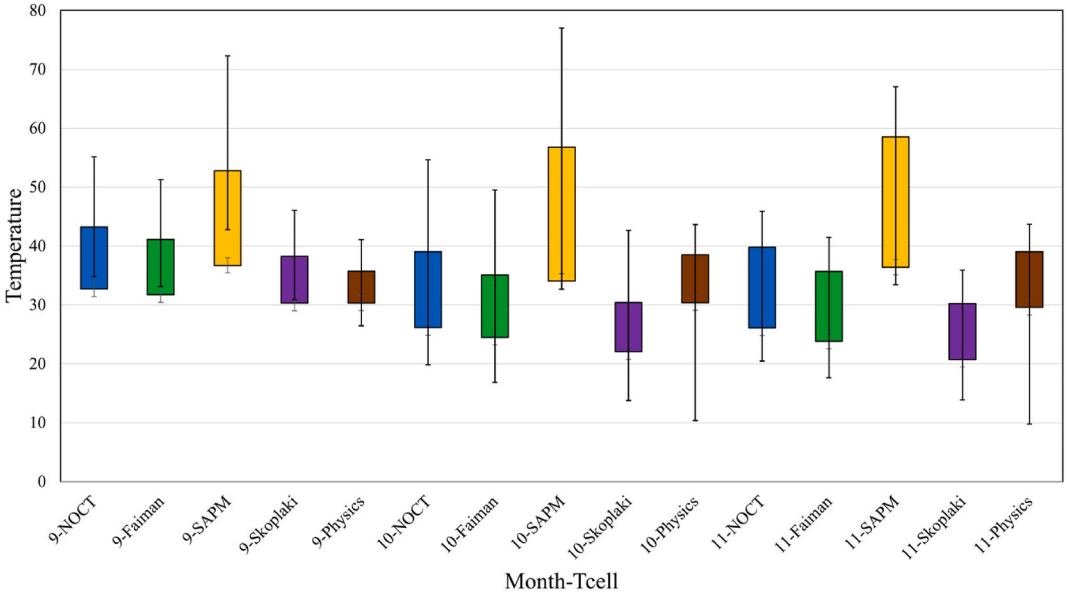

(c) Monthly averaged cell temperature

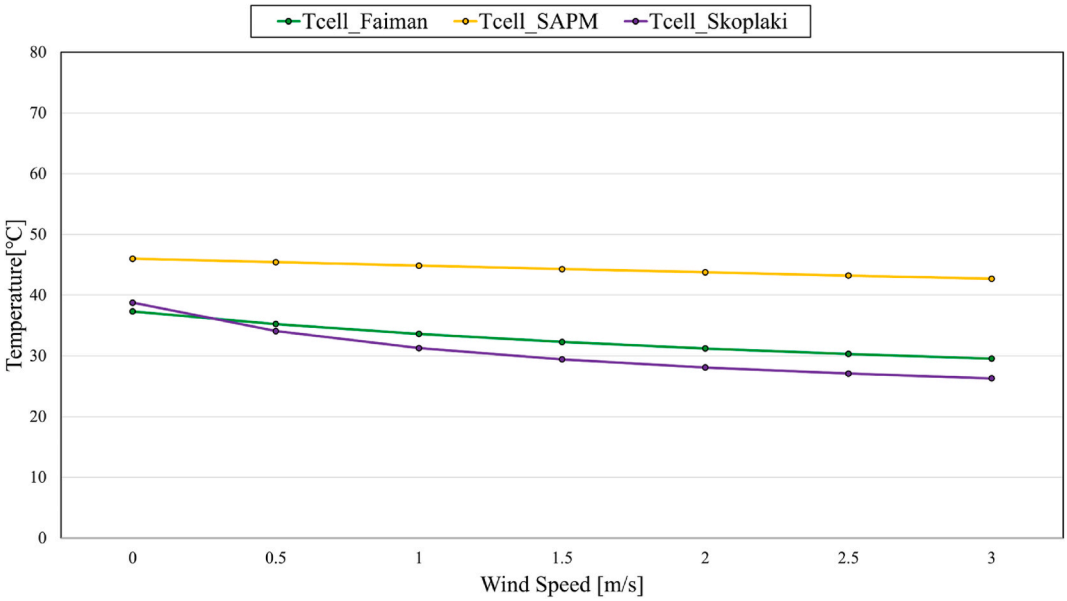

(d) Wind speed sensitivity of predicted cell temperature

Fig. 10. (*continued*).

and predicted outlet temperature were comparatively validated using R^2.

Fig. 12(a) shows the monthly cumulative power generation. In September, the measured power generation was 12.8 kWh, and the physics-based cell temperature model most closely predicted this value at 15.7 kWh. In October, the measured power generation was 46.5 kWh, and the physics-based cell/outlet temperature prediction model most closely predicted this value at 48.0 kWh, showing the closest agreement among all models. In November, the measured power generation was 28.6 kWh, and the physics-based model again provided the closest prediction at 29.6 kWh. Across all three months, the physics-based model achieved the lowest monthly RMSE of 2.01 kWh/month $(R^2 = 0.979)$, surpassing all the other cell temperature models.

These results confirm that accurate BIPVT power prediction requires explicit modeling of the heat-transfer fluid temperature effects on cell temperature.

Fig. 12(b) shows the total cumulative power generation over the full three-month period. The total measured power generation was 87.9 kWh, and the physics-based model predicted a value of 93.4 kWh yielding the lowest cumulative error of 6.3%. Furthermore, per evaluations on an hourly basis, the physics-based model achieved an RMSE of 0.022 kWh and an R^2 of 0.989, demonstrating superior time-series tracking accuracy as compared to that of the NOCT $(R^2 = 0.975)$, Faiman $(R^2 = 0.970)$, SAPM $(R^2 = 0.986)$, and Skoplaki $(R^2 = 0.962)$, models.

Fig. 13(a) shows the monthly cumulative thermal energy collection. In September, the measured thermal energy collection was

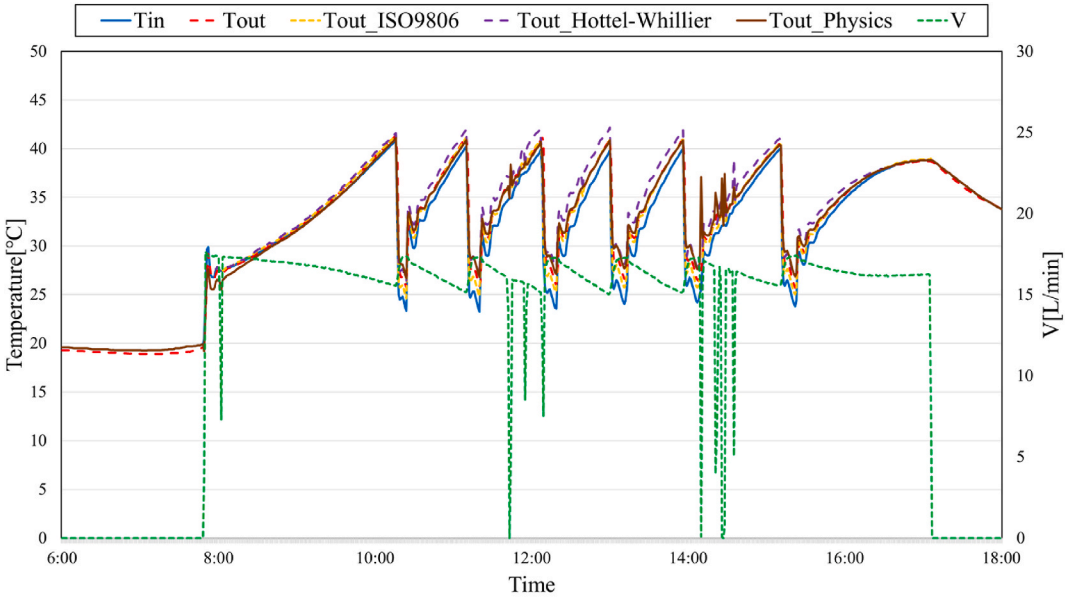

(a) Minute-resolution inlet and outlet fluid temperature profile

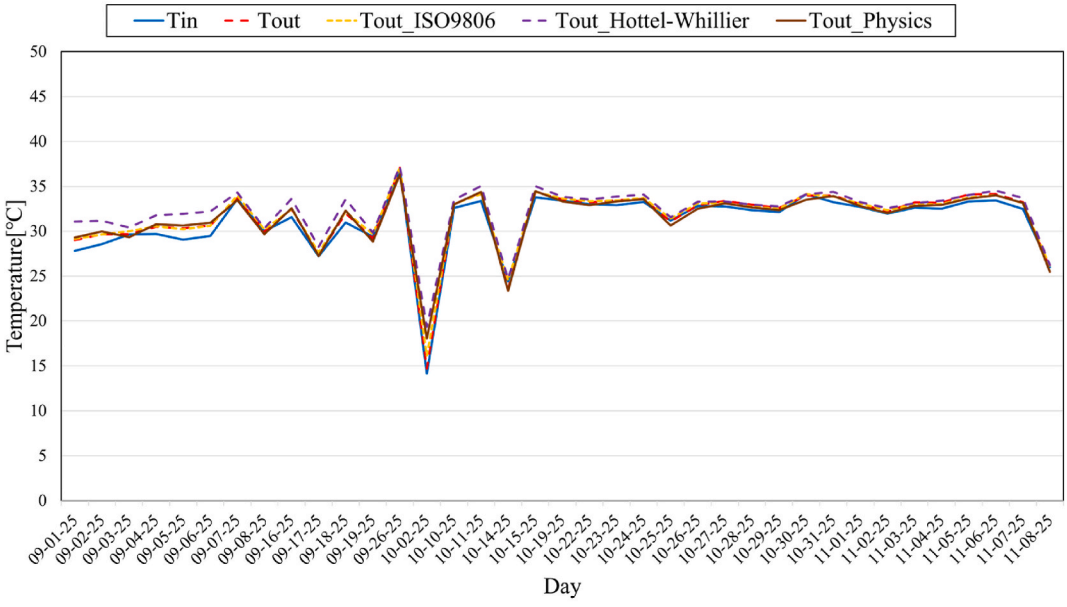

(b) Daily averaged inlet and outlet fluid temperature

Fig. 11. Measured outlet temperature and predicted outlet temperature

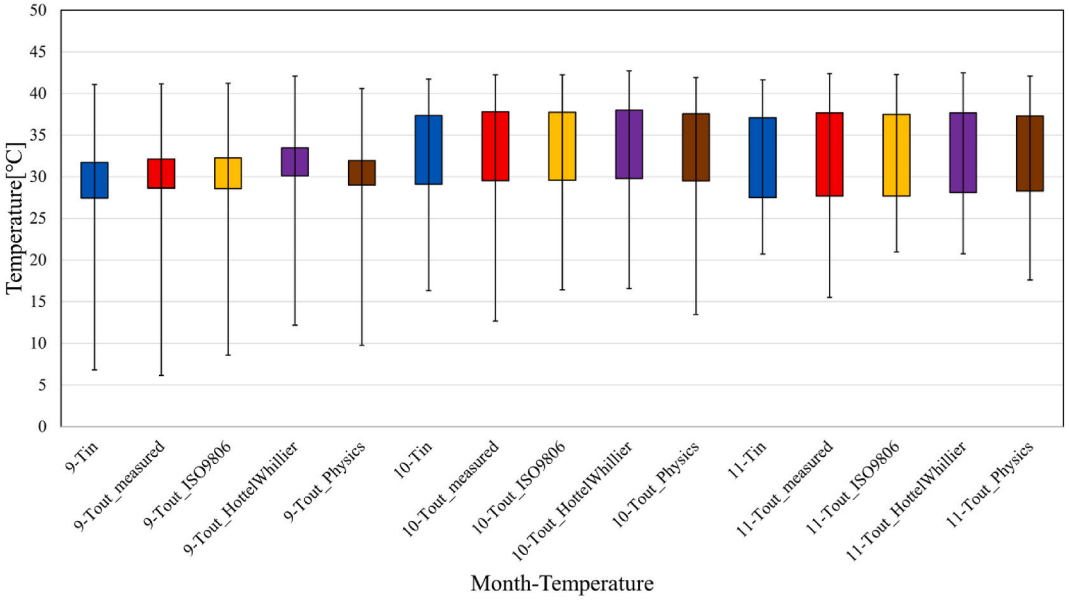

(c) Monthly averaged inlet and outlet fluid temperature

Fig. 11. (*continued*).

31.8 kWh, and the model most closely predicting this value was the ISO 9806 model, with a value of 31.8 kWh. In October, the measured thermal energy collection was 54.1 kWh, and the physics-based model predicted a value of 54.4 kWh, showing the closest agreement. In November, the measured thermal energy collection was 33.8 kWh, and the physics-based model predicted a value of 28.2 kWh. Among the three thermal models evaluated monthly, the physics-based model achieved the lowest RMSE of 5.14 kWh/month $(R^2 = 0.742)$, whereas the Hottel–Whillier model exhibited severely degraded performance with a monthly R^2 of −7.57, indicating predictions substantially worse than the measured mean a result attributable to systematic overestimation of thermal energy collection.

Fig. 13(b) shows the total cumulative thermal energy collection. The total measured thermal energy was 119.6 kWh. The physics-based predicted 121.2 kWh yielding the lowest total error rate of 1.3%. The ISO 9806 model underestimated production at 100.0 kWh (−16.4%), whereas the Hottel–Whillier model severely overestimated it at 196.8 kWh (+64.5%).

For the proposed physics-based cell/outlet temperature prediction model, which most accurately predicted the thermal energy collection, the predicted outlet temperature was comparatively validated against the measured outlet temperature using the R^2. Fig. 14 shows the correlation plot of the outlet temperatures. The correlation analysis yielded an R^2 value of 0.976, indicating that the model reproduced 97.6% of the variability in the outlet temperature. This result implies a high degree of linear agreement between the predicted and measured values and serves as evidence that the thermal energy collection calculated using the predicted outlet temperature can reliably reproduce the measured thermal energy collection.

4.4. Discussion

Herein, the prediction accuracy for electrical power generation and thermal energy collection of a BIPVT system was validated using existing respective models. Moreover, a model capable of predicting changes in power generation and thermal collection associated with cell temperature variations in BIPVT systems was proposed, and the resulting differences were interpreted in terms of how they appeared as deviations in monthly and total power generation predictions. From the comparison of total power generation, the measured value was 87.9 kWh, whereas the predicted values were 102.1 kWh (+16.2%) for the NOCT model, 103.7 kWh (+18.0%) for the Faiman model, 94.9 kWh (+8.0%) for the SAPM, 105.9 kWh (+20.6%) for the Skoplaki model, and 93.4 kWh (+6.3%) for the proposed physics-based model. Thus, the power generation prediction model employing the physics-based cell temperature model showed the smallest deviation in cumulative power generation. These results indicated that all the simplified cell temperature models systematically overestimated power generation under the vertical-plane BIPVT installation conditions of this study. This overestimation arose because the simplified models were originally developed and calibrated for conventionally tilted PV systems, and they consequently failed to fully capture the combined effects of reduced effective irradiance on a vertical façade and the modified thermal dynamics introduced by the fluid-coupled heat extraction layer in the BIPVT configuration. The proposed physics-based model, directly solving the coupled heat balance equations for the cell and fluid, reproduced these site-specific thermal conditions more faithfully, resulting in the closest agreement with the measured cumulative output.

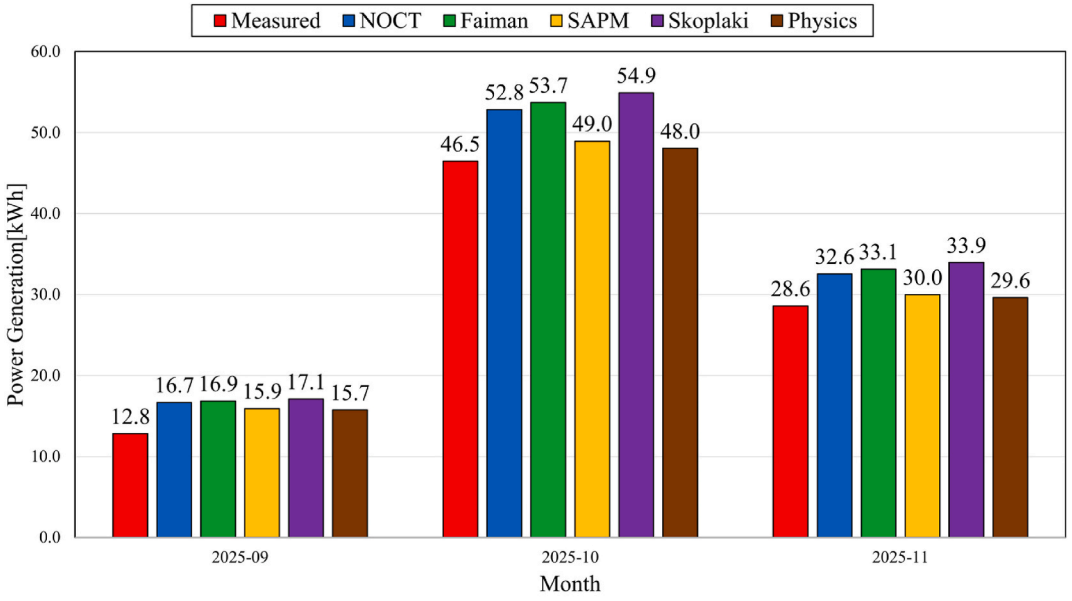

(a) Monthly power generation difference

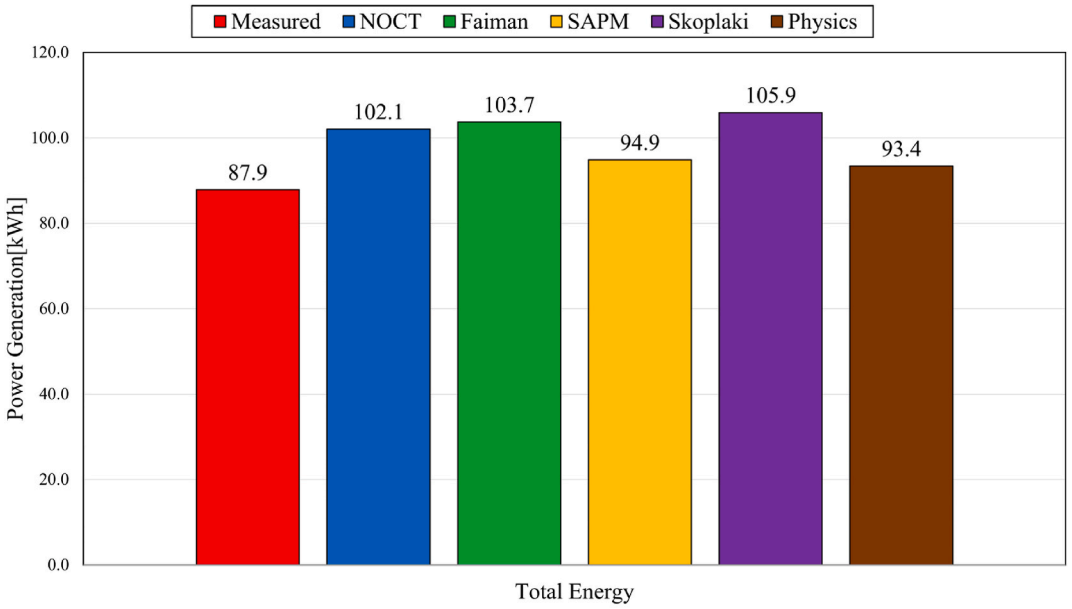

(b) Total power generation difference

Fig. 12. Comparison of power generation.

In terms of thermal performance, the outlet temperature increased during operating periods with fluid flow and under high-irradiance conditions, leading to thermal energy collection. Among the thermal collection prediction models, the physics-based model enabled direct calculation of the outlet temperature through heat balance equations, whereas the ISO 9806 and Hottel–-Whillier models are performance-based models for the calculation of useful thermal energy and cannot directly predict outlet temperature. Therefore, for the ISO 9806 and Hottel–Whillier models, the outlet temperature was obtained by back-calculating from the calculated useful thermal energy. From the comparison of total cumulative thermal energy, the measured value was 113.08 kWh, whereas the predicted values were 196.8 kWh (+64.5%) for the Hottel–Whillier model, 100.0 kWh (−16.4%) for the ISO 9806 model, and 121.2 kWh (+1.3%) for the physics-based model. The large overestimation by the Hottel–Whillier model (+64.5%) reflected the

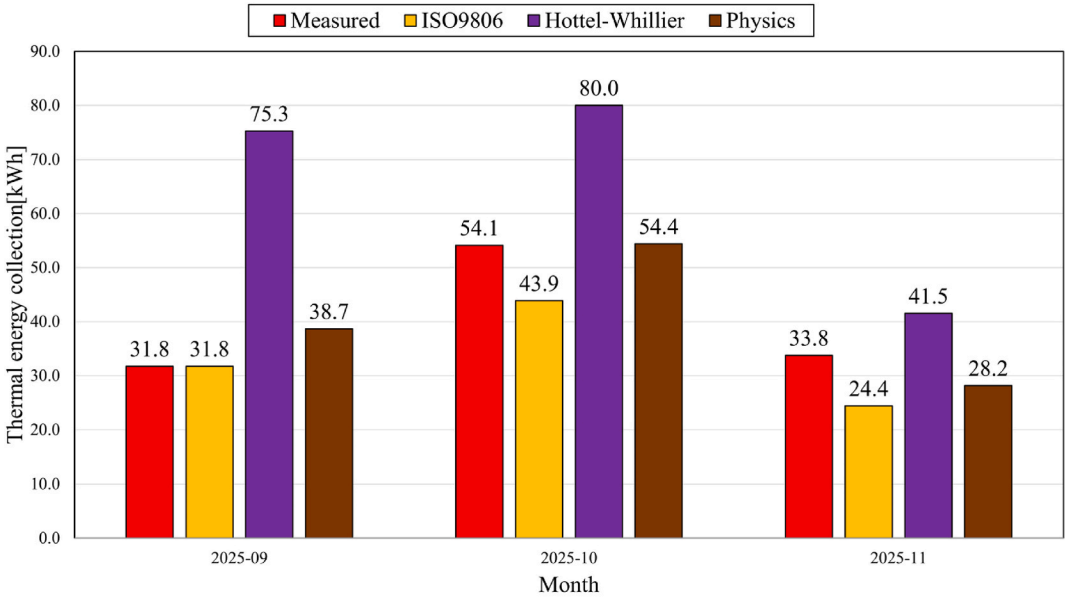

(a) Monthly thermal energy collection

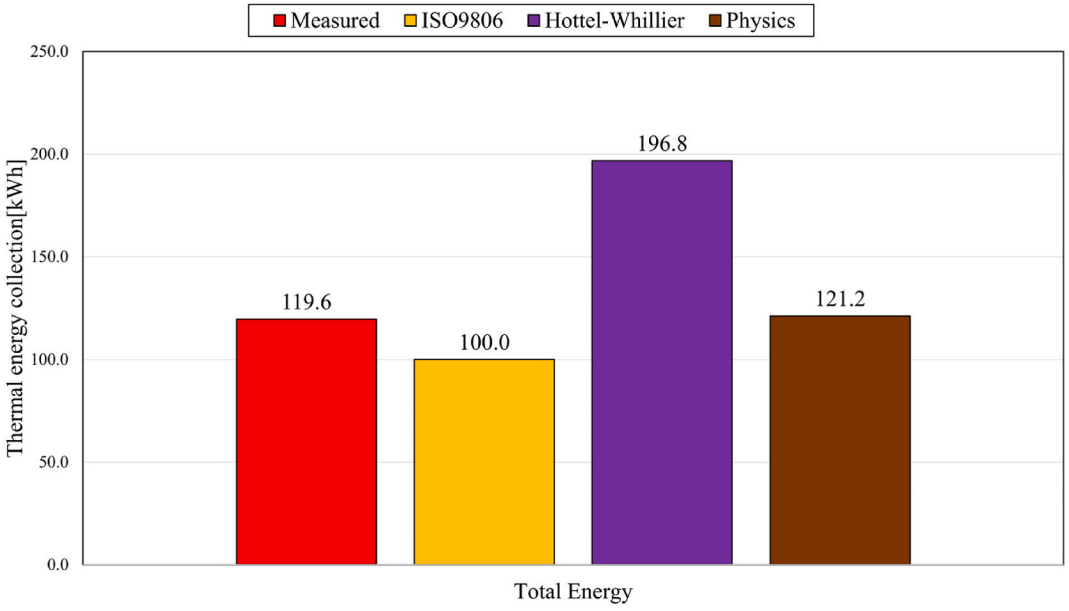

(b) Total thermal energy collection difference

Fig. 13. Comparison of thermal energy collection.

inherent limitation of back-calculating outlet temperature from a performance-coefficient-based formulation that was not designed for the high-angle thermal loss conditions of a vertical BIPVT façade; the resulting monthly R^2 of −7.57 further confirmed that this approach was unsuitable for the present configuration.

Accordingly, the thermal energy prediction using the physics-based outlet temperature model showed the smallest deviation in cumulative thermal energy. This suggests that under vertical-plane BIPVT conditions, actual thermal losses may not be adequately reflected in simplified performance-coefficient-based models.

The prediction errors observed herein are largely consistent with those reported in prior BIPVT validation studies, while also highlighting configuration-specific deviations attributable to vertical façade installation. In this context, Herrando et al. [40] reported

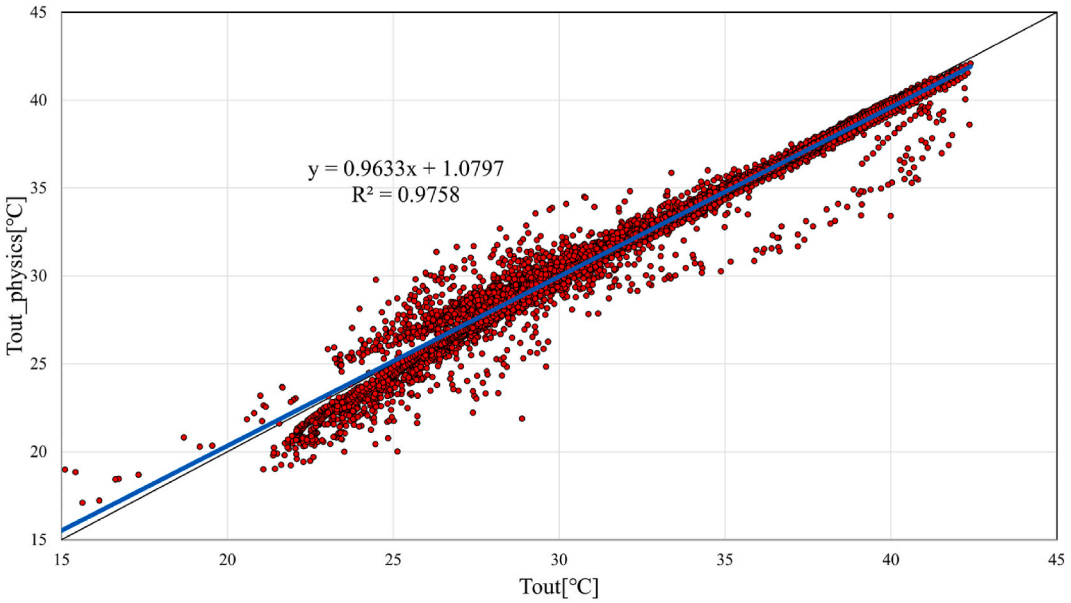

Fig. 14. Outlet temperature correlation.

cumulative thermal errors of approximately 8%–15% for Hottel–Whillier-based models applied to roof-mounted BIPVT systems, whereas this study recorded a substantially larger error of +64.5% under vertical installation, underscoring that performance-coefficient models are particularly sensitive to incidence angle and thermal boundary conditions. For power generation, the physics-based model error of +6.3% is comparable to the ±5%–10% range reported for coupled electrothermal models in façade-integrated PV systems [41], suggesting that the proposed model generalizes well despite the non-standard geometry. The SAPM, which yielded +8.0% total error herein, has been previously shown to yield errors in the 5%–12% range for building-integrated configurations in temperate climates [39], in reasonable agreement with the present results. These comparisons collectively affirm that physics-based coupled models are more robust across diverse installation geometries than simplified empirical or performance-coefficient alternatives.

The measured and modeled thermal results reveal non-negligible spatial temperature gradients across the BIPVT array, which carry direct implications for system design. The pronounced cell temperature peaks observed during high-irradiance periods reaching up to 60.7 °C (SAPM) in the simulation indicate that non-uniform heat flux distribution across the panel can induce local hotspots if the MFHP array is not spatially matched to the irradiance profile. Herein, the MFHP placement was determined on the basis of a uniform heat extraction assumption; however, the modeled temperature gradients suggest that concentrating heat pipe density toward the upper and center regions of the panel, where irradiance-induced temperatures are highest, could reduce peak cell temperature and improve both power and thermal yield.

In terms of manifold sizing and flow rate, the back-calculated outlet temperatures from the physics-based model indicate that the current flow rate is adequate for maintaining outlet temperatures within the 28–42 °C range observed across the validation period; however, flow rate modulation—i.e., reducing flow during low-irradiance periods to increase outlet temperature for useful heat delivery could be considered for practical control strategies. Array-level control based on predicted outlet temperature gradients, rather than a fixed flow schedule, would allow for the system to dynamically balance thermal extraction and electrical efficiency, particularly under the variable irradiance conditions characteristic of vertical façade exposure.

Since the physics-based model proposed in this study accounts for multi-layer heat conduction and heat exchange between the tube and the fluid, the mathematical structure of the model itself is not seasonally dependent and can be applied even under high-temperature and high-solar-irradiation conditions in summer. However, vertical BIPVT systems experience an increase in PV temperature and cooling load during the summer, and in façade-based BIPVT operation, reducing the cooling load and suppressing overheating have been identified as critical issues [5,6]. Therefore, when applying the model from this study during the summer, errors in power generation and heat collection predictions may increase due to the increased nonlinearity of radiative heat loss resulting from rising module and fluid temperatures, changes in flow control conditions, and the potential for thermal stagnation. In particular, since the parameters used in this study were validated under actual measurement conditions from September to November 2025 (fall and early winter), it is difficult to assume the same generalizability for high-temperature and high-solar-irradiation conditions during the summer.

Additionally, a wind speed sensitivity analysis was conducted to examine the impact of wind speed on model predictions. Since no on-site wind speed measurements were available for this study, the monthly average wind speed of 2.0 m/s from a weather station was used as the reference value, and the wind speed was varied in 0.5 m/s increments within the range of 0.0 to 3.0 m/s. As a result, the average cell temperature decreased from 37.3 °C to 29.5 °C in the Faiman model, from 46.0 °C to 42.7 °C in the SAPM model, and from

38.8 °C to 26.3 °C in the Skoplaki model. Under the same conditions, as the wind speed varied from 0.5 m/s to 3.0 m/s, the total power generation changed as follows: Faiman increased from 99.4 kWh to 104.9 kWh, SAPM increased from 93.3 kWh to 95.6 kWh, and Skoplaki from 98.4 kWh to 107.2 kWh, respectively, showing variations of up to +5.6% and −4.2%, +2.5% and −1.7%, and +8.9% and −7.1% compared to the reference wind speed of 2.0 m/s. Therefore, using the average wind speed from a weather station as a substitute value may result in relatively small deviations in electricity output predictions. Meanwhile, heat collection forecasts were sensitive to wind speed inputs; however, it was difficult to fully reproduce the temporal variability of actual operating conditions using only representative values such as monthly or daily averages. Therefore, in future research, it is advisable to recalibrate the model using high-temporal-resolution wind speed data and expand it to reflect dynamic operating conditions.

Furthermore, spatial temperature inhomogeneities within the panel represent a structural limitation of the lumped-parameter model. Although this study did not install distributed temperature sensors and thus could not directly measure the local temperature field, considering the thermal imaging analysis results from a previous study [13], it is highly likely that a vertical temperature gradient exists within the panel. Therefore, while the lumped-parameter model used in this study is suitable for predicting global thermal behavior by averaging out such local inhomogeneities, it has limitations in accurately reproducing local hotspots or detailed temperature distributions.

In summary, under the conditions of this study, the physics-based model exhibited the smallest deviations for both power generation and thermal energy prediction (+6.3% for power generation and +1.3% for thermal energy), indicating that this model is optimal for reproducing the measured values. However, for practical building applications or long-term predictions based on certified data, the availability of detailed input information such as internal module structural data, may be limited. In such cases, a combination of the Faiman model–which features relatively low input requirements and simple implementation for power generation prediction (+9.7%)–and the ISO 9806 model for thermal energy prediction (−16.4%), which, despite underestimating thermal output, avoids the extreme overestimation exhibited by the Hottel–Whillier model and requires only standardized collector performance parameters, may represent a more practical approach for applications relying on certified datasets.

5. Conclusion

This study involved an analysis of the electrical and thermal performance of frameless curtain-wall type BIPVT modules installed on the south-facing envelope of the KePSH-2 building at the Korea Institute of Energy Research in Daejeon, Republic of Korea, using measured data recorded at 1-min intervals from 1 September to 8 November 2025. During the experimental period, the instantaneous electrical power of the BIPVT system peaked at approximately 1100 W, and the instantaneous thermal energy collection peaked at 9049.8 W under clear-sky conditions. Daily, the power generation ranged from 0.00 to 6.2 kWh/day, and the thermal energy collection ranged from 0.00 to 9.5 kWh/day. Over the entire period, the cumulative power generation and thermal collection were 87.9 kWh and 119.6 kWh, respectively.

The measured data were leveraged to apply four power generation prediction models and two thermal collection prediction models under identical operating conditions. In addition, a physics-based cell/outlet temperature prediction model that directly incorporated multilayer conductive thermal resistance and heat transfer between the copper tube and the heat transfer fluid was proposed, and the predicted results were comparatively validated against the measured data. The analysis showed that, in the monthly comparison, the physics-based model provided the closest predictions across all three months for power generation. For thermal energy collection, the ISO 9806 model showed the closest prediction in September, whereas the physics-based model showed the closest predictions in October and November. On a total cumulative basis, the proposed physics-based cell/outlet temperature model predicted 93.4 kWh of power generation with an error rate of +6.3%, and 121.2 kWh of thermal energy with an error rate of +1.3%, indicating the lowest error rates among the evaluated power generation and thermal collection prediction models. Moreover, the outlet temperature correlation analysis yielded an R^2 value of 0.976, demonstrating a high degree of linear agreement and confirming that the physics-based model successfully reproduces outlet temperature variations.

Beyond the quantitative comparison of individual model outputs, these results reveal two generalizable mechanisms that govern prediction accuracy in curtain-wall-type liquid BIPVT systems. First, simplified empirical cell temperature models systematically overestimate power generation under vertical-façade BIPVT conditions, because they were originally calibrated for conventionally tilted PV systems and do not factor in the reduced effective irradiance on vertical surfaces nor the active cell cooling introduced by the circulating heat transfer fluid. This structural mismatch produces a consistent positive bias in predicted power output that grows with deviation from standard installation geometry. Second, performance-coefficient-based thermal energy collection models originally derived from flat-plate collector experiments at near-optimal tilt angles exhibit substantially amplified prediction errors when applied to vertical BIPVT configurations, where high solar incidence angles and wall-side insulation boundary conditions fundamentally alter the thermal loss characteristics. The cumulative overestimation of +64.5% and a monthly R^2 of −7.57 yielded using the Hottel–-Whililer model in this study are direct consequences of such a mismatch. These findings establish a general rule: for BIPVT systems installed at non-standard orientations with integrated fluid heat extraction, physics-based models that explicitly resolve multilayer heat conduction and in-tube convection are necessary to simultaneously and reliably predict both electrical and thermal output. This constitutes the primary novelty of the proposed model providing an experimentally validated, physically interpretable predictive framework applicable to curtain-wall BIPVT configurations that existing empirical and performance-coefficient approaches cannot adequately address.

Our results indicate that an approach incorporating multilayer heat conduction and in-tube convection/heat exchange mechanisms in curtain-wall-type liquid BIPVT systems provides experimentally grounded evidence applicable to the prediction of electrical and thermal energy collection, estimation of thermal supply coupled with thermal source equipment, and the assessment of energy self-

sufficiency and system capacity in future building applications of BIPVT.

From a practical application perspective, in terms of power generation forecasting, the physics-based model demonstrated the highest accuracy under the vertical curtain wall BIPVT conditions examined in this study, making it the most suitable for precise performance evaluation and design review. Among empirical models with limited input data, SAPM can serve as a practical alternative, as it offers both a relatively simple input structure and stable forecasting performance. NOCT and Faiman are advantageous for rapid performance evaluation due to their simple implementation and low computational burden; however, under the conditions of this study, they exhibited a relatively significant tendency to overestimate, limiting their suitability for precise design. Skoplaki has the advantage of being able to account for wind speed effects; however, its heavy reliance on wind speed data means that prediction stability may decrease if on-site wind speed data is unavailable. For heat collection rate prediction, physics-based models proved most suitable; however, ISO 9806 can be used as an alternative when only the collector performance coefficient is available. In contrast, the Hottel–Whillier model does not sufficiently account for the heat loss characteristics of vertical BIPVTs and is therefore not suitable for the conditions of this study.

However, this study has several limitations. First, although some empirical models require wind speed as an input variable, wind speed measurements were not available in this experiment. Therefore, while comparative analysis among models is possible, the generalization of results for models sensitive to wind speed variations is limited. Second, the experimental period herein was confined to September through November, and additional validation is required to assess applicability under summer overheating and stagnation conditions as well as winter low-temperature and low-irradiance conditions. Moreover, extending the analysis to year-round long-term operation data and incorporating seasonal operating strategies from a building thermal operation perspective would enable further research into optimal control and system design, thereby enhancing the applicability of BIPVT systems to zero-energy buildings.

CRediT authorship contribution statement

Heon-Min Lee: Writing – original draft, Formal analysis, Conceptualization. **Youngsub An:** Resources, Data curation. **Ye-Bin Shin:** Software, Methodology. **Wong-Jong Choi:** Software, Resources. **ByungKi Jeon:** Visualization, Validation. **Jongkyu Kim:** Project administration, Funding acquisition. **Jae-Weon Jeong:** Writing – review & editing, Supervision. **Min-Hwi Kim:** Supervision, Project administration, Funding acquisition.

Declaration of competing interest

The authors declare that they have no known competing financial interests or personal relationships that could have appeared to influence the work reported in this paper.

Acknowledgement

This study was conducted under the framework of the Research and Development Program of the Korea Institute of Energy Research (C6-2410-32) and supported by a Korea Agency for Infrastructure Technology Advancement (KAIA) grant funded by the Ministry of Land, Infrastructure and Transport (Grant RS-2025-02316198).

Data availability

The authors do not have permission to share data.

References

[1] D. Ürge-Vorsatz, K. Petrichenko, M. Staniec, J. Eom, Energy use in buildings in a long-term perspective, Curr. Opin. Environ. Sustain. 5 (2) (2013) 141–151.
[2] Y. Kim, J. Yu, D.W. Cho, S. Tae, Study on the certification policy of zero-energy buildings in Korea, Sustainability 12 (12) (2020) 5172, https://doi.org/10.3390/su12125172.
[3] Ministry of Environment (Republic of Korea), Fourth Biennial Update Report of the Republic of Korea Under the United Nations Framework Convention on Climate Change (UNFCCC), UNFCCC, Bonn, 2021, pp. 53–54. (Accessed 6 February 2026).
[4] Samah Mehira, Aicha Boussoualim, Comprehensive Review of Building Integrated Photovoltaic and Thermal Systems, BIPV/T), 2025, https://doi.org/10.18280/ijepm.100207.
[5] A.S. Abdelrazik, B. Shboul, M. Elwardany, R.N. Zohny, A. Osama, The recent advancements in the building integrated photovoltaic/thermal (BIPV/T) systems: an updated review, Renew. Sustain. Energy Rev. 170 (2022) 112988, https://doi.org/10.1016/j.rser.2022.112988.
[6] M. Chandrasekar, Building-integrated solar photovoltaic thermal (BIPVT) technology: a review on the design innovations, aesthetic values, performance limits, storage options and policies, Adv. Build. Energy Res. 17 (2) (2023) 223–254, https://doi.org/10.1080/17512549.2023.2185675.
[7] K. Bot, D. Aelenei, H. Gonçalves, C.S. Silva, Experimental assessment of a liquid BIPVT system under Mediterranean conditions, Energies 14 (8) (2021) 2191, https://doi.org/10.3390/en14082191.
[8] J. Oh, S. Bae, H. Chae, Y. Nam, Experimental study on the thermal and electric energy performance for wall-type BIPVT system, Korean J. Air-Cond, Refrig. Eng. 36 (9) (2024) 474–479, https://doi.org/10.6110/KJACR.2024.36.9.474.
[9] R.G. Ross Jr., Interface design considerations for terrestrial solar cell modules, in: Proc. 12th IEEE Photovoltaic Specialists Conference (PVSC), 1976, pp. 801–806. Baton Rouge, LA, USA.
[10] N. Martín-Chivelet, J. Polo, C. Sanz-Saiz, L.T. Núñez Benítez, M. Alonso-Abella, J. Cuenca, Assessment of PV module temperature models for building-integrated photovoltaics (BIPV), Sustainability 14 (3) (2022) 1500, https://doi.org/10.3390/su14031500.
[11] N. Martín-Chivelet, J. Polo, C. Sanz-Saiz, L.T. Núñez Benítez, M. Alonso-Abella, J. Cuenca, Assessment of PV module temperature models for building-integrated photovoltaics (BIPV), Sustainability 14 (3) (2022) 1500, https://doi.org/10.3390/su14031500.

[12] Y. An, W. Lee, H.J. Joo, D.W. Kim, J. Kim, M.H. Kim, Effects of heat collection methods on the electrical and thermal efficiencies of building-integrated photovoltaic thermal modules, Appl. Therm. Eng. 277 (2025) 127067, https://doi.org/10.1016/j.applthermaleng.2025.127067.
[13] Y.B. Shin, H.M. Lee, W.J. Choi, D.W. Kim, Y. An, W. Lee, et al., Development of a frameless building-integrated photovoltaic thermal system with phase change material, Appl. Therm. Eng. (2025) 128716, https://doi.org/10.1016/j.applthermaleng.2025.128716.
[14] International Organization for Standardization (ISO), ISO 9806:2017 Solar Energy - Solar Thermal Collectors - Test Methods, ISO, Geneva, 2017.
[15] H.C. Hottel, A. Whillier, Evaluation of flat-plate solar collector performance, Trans. Conf. Use Sol. Energy 3 (1955). Thermal Processes, Part 2, https://www.osti.gov/biblio/5057828. (Accessed 6 February 2026).
[16] F.J. González Gallero, I. Rodríguez Maestre, G. González Siles, J.L. Foncubierta Blázquez, M. Bottarelli, Performance analysis of a novel façade-based building integrated photovoltaic-thermal system with phase change material for domestic hot water, Appl. Therm. Eng. 240 (2024) 122321, https://doi.org/10.1016/j.applthermaleng.2023.122321.
[17] M. Babin, N.L. Andersen, J.K. Thorning, S. Thorsteinsson, Yield analysis of a BIPV façade prototype installation, Energy Build. 322 (2024) 114730, https://doi.org/10.1016/j.enbuild.2024.114730.
[18] P. Hazarika, Shyam, P. Kalita, A. Gaur, Annual energy analysis of a building-integrated semitransparent photovoltaic thermal façade, J. Sol. Energy Eng. 147 (3) (2025) 034501, https://doi.org/10.1115/1.4067371.
[19] M. Valinejadshoubi, A.-M. Sigounis, A.K. Athienitis, A. Bagchi, Switchable building-integrated photovoltaic–thermal curtain Wall for building integration, Processes 13 (8) (2025) 2512, https://doi.org/10.3390/pr13082512.
[20] N. Albinius, B. Rau, M. Riedel, C. Ulbrich, A comprehensive case Study of a full-size BIPV facade, Energies 18 (5) (2025) 1293, https://doi.org/10.3390/en18051293.
[21] G. Mangherini, V. Diolaiti, P. Bernardoni, A. Andreoli, D. Vincenzi, Review of façade photovoltaic solutions for less energy-hungry buildings, Energies 16 (19) (2023) 6901, https://doi.org/10.3390/en16196901.
[22] D. Faiman, Assessing the outdoor operating temperature of photovoltaic modules, Prog. Photovolt. Res. Appl. 16 (4) (2008) 307–315, https://doi.org/10.1002/pip.813.
[23] D.L. King, W.E. Boyson, J.A. Kratochvil, Photovoltaic Array Performance Model, Sandia National Laboratories, Albuquerque, NM, 2004, https://doi.org/10.2172/919131. Report No. SAND2004-3535.
[24] E. Skoplaki, J.A. Palyvos, Operating temperature of photovoltaic modules: a survey of pertinent correlations, Renew. Energy 34 (1) (2009) 23–29, https://doi.org/10.1016/j.renene.2008.04.009.
[25] S.S. Park, Y.J. Kim, E.C. Kang, E.J. Lee, Numerical investigations of solar energy heat transfer performances with experimental validations in a water-based serpentine photovoltaic-thermal (PVT) collector, J. Therm. Anal. Calorim. 148 (2023) 2149–2169, https://doi.org/10.1007/s10973-022-11861-z.
[26] L.W. Florschuetz, Extension of the Hottel-Whillier model to the analysis of combined photovoltaic/thermal flat plate collectors, Sol. Energy 22 (1979) 361–366, https://doi.org/10.1016/0038-092X(79)90190-7.
[27] International Electrotechnical Commission (IEC), IEC 60904-3:2019 Photovoltaic Devices - Part 3: Measurement Principles for Terrestrial Photovoltaic (PV) Solar Devices with Reference Spectral Irradiance Data, IEC, Geneva, 2019.
[28] M. Koehl, M. Heck, S. Wiesmeier, J. Wirth, Modeling of the nominal operating cell temperature based on outdoor weathering, Sol. Energy Mater. Sol. Cells 95 (7) (2011) 1638–1646, https://doi.org/10.1016/j.solmat.2011.01.030.
[29] International Electrotechnical Commission (IEC), IEC 61215-1:2021 Terrestrial Photovoltaic (PV) Modules - Design Qualification and Type Approval - Part 1: Test Requirements, IEC, Geneva, 2021.
[30] Korea Meteorological Administration (KMA), Climate statistics: monthly mean wind speed (Daejeon, Republic of Korea) (ASOS climatological normals), KMA, Seoul. https://data.kma.go.kr. (Accessed 6 February 2026).
[31] ASHRAE, ASHRAE Handbook - Fundamentals, ASHRAE, Atlanta, GA, 2021.
[32] K. Kramer, S. Mehnert, C. Thoma, P. Ollas, Guide to Standard ISO 9806:2017 2.0: a Resource for Manufacturers, Testing Laboratories, Certification Bodies and Regulatory Agencies, IEA SHC, 2018.
[33] J.A. Duffie, W.A. Beckman, Solar Engineering of Thermal Processes, fourth ed., Wiley, Hoboken, NJ, 2013.
[34] Å. Melinder, Thermophysical Properties of Aqueous Solutions Used as Secondary Working Fluids, Royal Institute of Technology (KTH), Stockholm, 2007.
[35] F.P. Incropera, D.P. DeWitt, T.L. Bergman, A.S. Lavine, Fundamentals of Heat and Mass Transfer, eighth ed., Wiley, Hoboken, NJ, 2017.
[36] S.C. Chapra, R.P. Canale, Numerical Methods for Engineers, seventh ed., McGraw-Hill Education, New York, NY, 2015.
[37] F.W. Dittus, L.M.K. Boelter, Heat transfer in automobile radiators of the tubular type, Univ. Calif. Publ. Entomol. 2 (1930) 443–461.
[38] E.W. Lemmon, I.H. Bell, M.L. Huber, M.O. McLinden, NIST Standard Reference Database 23: Reference Fluid Thermodynamic and Transport Properties - REFPROP, National Institute of Standards and Technology, Gaithersburg, MD, 2018, https://doi.org/10.18434/T4/1502528, Version 10.0.
[39] S.J. Kline, F.A. McClintock, Describing uncertainties in single-sample experiments, Mech. Eng. 75 (1) (1953) 3–8.
[40] M. Herrando, C.N. Markides, K. Hellgardt, A UK-based assessment of hybrid PV and solar-thermal systems for domestic heating and power: system performance, Appl. Energy 122 (2014) 288–309, https://doi.org/10.1016/j.apenergy.2014.01.061.
[41] E. Kaplani, S. Kaplanis, Dynamic electro-thermal PV temperature and power output prediction model for any PV geometries in free-standing and BIPV systems operating under any environmental conditions, Energies 13 (18) (2020) 4743, https://doi.org/10.3390/en13184743.